Semaphorin7A patterns neural circuitry in the lateral line of the zebrafish

Agnik Dasgupta[1,*], Caleb C. Reagor[1,2], Sang P. Paik[1,3], Lauren M. Snow[1,4], Adrian Jacobo[1,5], and A. J. Hudspeth[1]

[1] Howard Hughes Medical Institute and Laboratory of Sensory Neuroscience, The Rockefeller University, New York, NY, USA

*Corresponding author: Dr. Agnik Dasgupta
Laboratory of Sensory Neuroscience
The Rockefeller University
New York, NY 10065
Telephone: 212-327-7353
E-mail: adasgupta@rockefeller.edu

[2] Tri-Institutional PhD Program in Computational Biology and Medicine, New York, NY, USA

[3] Present address: Department of Functional Neuroanatomy, Institute for Anatomy and Cell Biology, Heidelberg University, Heidelberg, Germany

[4] Present address: Brigham and Women's Hospital, Boston, MA, USA

[5]Chan Zuckerberg Biohub San Francisco, San Francisco, CA, USA

Abstract

In a developing nervous system, axonal arbors often undergo complex rearrangements before neural circuits attain their final innervation topology. In the lateral line sensory system of the zebrafish, developing sensory axons reorganize their terminal arborization patterns to establish precise neural microcircuits around the mechanosensory hair cells. However, a quantitative understanding of the changes in the sensory arbor morphology and the regulators behind the microcircuit assembly remain enigmatic. Here, we report that Semaphorin7A (Sema7A) acts as an important mediator of these processes. Utilizing a semi-automated three-dimensional neurite tracing methodology and computational techniques, we have identified and quantitatively analyzed distinct topological features that shape the network in wild-type and Sema7A loss-of-function mutants. In contrast to those of wild-type animals, the sensory axons in Sema7A mutants display aberrant arborizations with disorganized network topology and diminished contacts to hair cells. Moreover, ectopic expression of a secreted form of Sema7A by non-hair cells induces chemotropic guidance of sensory axons. Our findings propose that Sema7A likely functions both as a juxtracrine and as a secreted cue to pattern neural circuitry during sensory organ development.

Introduction

Pathfinding axons are directed to their appropriate synaptic targets by a variety of guidance cues. While approaching or traversing the target field, the growth cones of migrating axons encounter secreted or cell surface-attached ligands and respond by steering toward or away from their sources (1–4). Fine-grained control of these factors is critical for the establishment of proper neural circuitry.

The zebrafish's lateral line provides a tractable *in vivo* system for exploring the mechanisms that guide the assembly of neural circuits in a peripheral nervous system. In particular, it is possible to detect individual hair cells and the sensory axons that innervate them throughout the first week of development (5). The primary posterior lateral line on each side of the zebrafish's tail consists of about seven neuromasts, which contain mechanoreceptive hair

46 cells of opposing polarities—half sensitive to headward (rostrad) water motion and the
47 complementary half to tailward (caudad) water motion—that cluster at their centers (6). The
48 sensory axons of the lateral-line nerve branch, arborize, and consolidate around the basolateral
49 surfaces of the hair cells (Figure 1A). To aid in an animal's swimming behavior, these hair cells
50 sense water currents and relay signals to the brain through the sensory axons (7). The well-
51 defined structure of the ramifications and synaptic contacts of the sensory axons highlight the
52 need to determine the molecular signals behind the assembly of such precise microcircuits (8).
53 We adopted a candidate-gene strategy to seek factors that direct the growth of afferent
54 growth cones in the zebrafish's lateral line. Analysis of single-cell RNA sequencing data
55 identified the *semaphorin7a* (*sema7a*) gene to be highly expressed in hair cells of that organ
56 (9). Semaphorins are important regulators of axonal growth and target finding during the
57 patterning of diverse neural circuits (10). The semaphorin family includes proteins that are
58 secreted, transmembrane, and cell surface-attached (11). Among these, Semaphorin7A
59 (Sema7A) is the only molecule that is anchored to the outer leaflet of the lipid bilayer of the cell
60 membrane by a glycosylphosphatidylinositol (GPI) linker (11). Unlike many other semaphorins,
61 which act as repulsive cues (12,13), Sema7A is involved in promoting axon growth (4) and
62 imparting directional signals by interacting with the integrin and plexin families of receptors
63 residing on the pathfinding axons (14–16). Sema7A likely occurs *in vivo* in both GPI-anchored
64 and soluble forms (17–19), and studies of neuronal explants confirm that both forms can induce
65 directed axonal outgrowth (4). Furthermore, it has been proposed that the GPI anchor is
66 cleaved by membrane-resident GPI-specific phospholipases (GPI-PLs) or matrix
67 metalloproteases to release the Sema7A into the extracellular environment and thus regulate
68 dynamic cellular processes (20,21). Because these observations indicate that Sema7A might
69 influence neuronal development both as a juxtracrine and as a diffusive signal, we investigated
70 the role of Sema7A in sculpting a vertebrate peripheral sensory organ.

71 **Results**

72 **Sema7A expression and localization in hair cells.** The zebrafish genome contains a single
73 *sema7a* gene that produces two transcripts. One transcript encodes Sema7A-GPI, a full-
74 length, GPI-linked, cell surface-attached protein. The second transcript yields Sema7A^{sec}, a
75 protein with a truncated C-terminus, which we conjecture is secreted into the local environment.
76 Each transcript encodes an N-terminal signal sequence and a single copy of the conserved
77 Sema domain (11). To detect the presence of both *sema7a* transcripts in the hair cells of the
78 lateral-line neuromasts, we used fluorescence-activated cell sorting (FACS) to capture the
79 labeled hair cells (22) and isolated total RNA. Using primers that flank the regions encoding
80 the conserved Sema domain and the distinct C-termini of the two transcripts, we performed
81 reverse transcription and polymerase chain reactions (RT-PCR) to identify both the membrane-
82 anchored and the secreted transcript in developing larvae (Figure 1B-D; Figure 1—figure
83 supplement 1A-D). Single-cell RNA sequencing data also have shown that the GPI-linked
84 *sema7a* transcript is particularly enriched in the immature and mature hair cells of the
85 neuromast during early larval development (9), a period when sensory axons of the posterior
86 lateral line contact hair cells and form synapses with them (5,23). Indeed, we have observed
87 Sema7A to be specifically localized in both mature and immature hair cells (Figure 1E; Figure
88 1—figure supplement 2A-D).

89 As neuromasts mature, the contacts between sensory axons and hair cells increase in
90 number, become stabilized, and establish synapses (5,23). Because Sema7A can modulate
91 axon guidance (4,14) and synapse formation (15), we wondered whether the level of Sema7A
92 also changes during neuromast development. Upon quantifying the average intensity of
93 Sema7A, we found similar expression in rostrally and caudally polarized hair cells of
94 neuromasts at 1.5, 2, 3, and 4 days post fertilization (dpf). The average Sema7A intensity
95 increased significantly over this period in both rostrally and caudally polarized hair cells. At
96 1.5 dpf, the neuromasts harbor primarily immature hair cells that make minimal contacts with
97 sensory axons and do not form stable association with axonal terminals (23). At this stage the
98 average Sema7A intensity in hair cells remained low. By 2-4 dpf the hair cells mature to form

99 stable contacts and well-defined synapses with the sensory axons (5,24). The average
100 Sema7A intensity in hair cells at each of these stages rose to levels that significantly exceeded
101 those of 1.5 dpf neuromasts (Figure 1F). This rise in the amount of Sema7A during neuromast
102 maturation supports a role for Sema7A in the guidance of sensory axons and their interaction
103 with hair cells.

104 We additionally demonstrated an anisotropic distribution of Sema7A along the
105 apicobasal axis of each hair cell. As neuromasts develop through 2, 3, and 4 dpf, Sema7A
106 remained highly enriched in the subapical region of the hair cell, the site of the Golgi network
107 (Figure 1E). This localization suggests that Sema7A—like other proteins of the semaphorin
108 family (25)—is directed to the plasmalemma through Golgi-mediated vesicular trafficking.
109 Using the transgenic line *Tg(cldnb:LY-mScarlet)* that expresses membrane-tethered mScarlet
110 in all cells of the neuromast (26), we detected Sema7A at the plasma membrane and potentially
111 in vesicles (Figure 1—figure supplement 2E-H). While Sema7A maintained a high level in the
112 subapical region, the protein increasingly accumulated at the base of the hair cell: the Sema7A
113 level at the hair cell base was low at 2 dpf, but increased sharply by 3 dpf and 4 dpf (Figure 1G;
114 Figure 1—figure supplement 1I,J). During this period the hair cells increase in number and
115 mature, whereas the associated sensory axons arborize to contact multiple hair cells and form
116 robust synaptic boutons at their bases (5,24). Does progressive basal accumulation of Sema7A
117 facilitate association of sensory axon terminals to the hair cell? To address this question, we
118 utilized doubly labeled transgenic fish *Tg(myo6b:actb1-EGFP;neurod1:tdTomato)* that marked
119 the hair cells and the sensory axons of the posterior lateral line with distinct fluorophores
120 (Figure 1A) (27). We quantified the average Sema7A intensity and the accumulation of sensory
121 arbors, measured by td-Tomato intensity, at the bases of the hair cells. Across developmental
122 stages, the basal association of the sensory arbors showed a positive correlation with Sema7A
123 accumulation (Figure 1H,I; Figure 1—figure supplement 3A-E, Video 1). The progressive
124 enrichment of Sema7A at the hair cell base with the sensory axons suggests that Sema7A acts
125 as a mediator of contacts between sensory axons and hair cells.

126 **Sema7A restricts sensory axons around clustered hair cells**. If Sema7A guides and
127 restricts the sensory arbors at and around the hair cells clustered in a neuromast, then
128 inactivating Sema7A function should disrupt this process. To test this hypothesis, we obtained
129 a *sema7a* mutant allele (*sema7a*^{sa24691}) with a point mutation that introduces a premature stop
130 codon in the conserved sema domain (Figure 2—figure supplement 1A). The homozygous
131 mutant, hereafter designated *sema7a*$^{-/-}$, should lack both the secreted and the membrane-
132 attached forms of Sema7A. The average intensity of Sema7A immunolabeling in hair cells
133 diminished by 61% in *sema7a*$^{-/-}$ larvae (0.34 ± 0.01 arbitrary units) in comparison to controls
134 (0.87 ± 0.01 arbitrary units). In a few cases we observed minute accumulations of Sema7A at
135 the subapical region, but little or no protein at the base of the mutant hair cells (Figure 2A;
136 Figure 2—figure supplement 1B). Furthermore, we tested the mechanotransduction ability of
137 *sema7a*$^{-/-}$ mutant hair cells by labeling with the styryl dye FM4-64 (5). The *sema7a*$^{-/-}$ larvae
138 incorporated the FM4-64 as effectively as the control animals. This result suggests that the
139 mutation does not impact essential hair cell functions (Figure 2—figure supplement 1C,D,
140 Videos 2,3).

141 To characterize the impact of the *sema7a*$^{-/-}$ mutation on arbor patterning, we utilized
142 doubly labeled transgenic fish *Tg(myo6b:actb1-EGFP;neurod1:tdTomato)* that distinctly
143 labeled the hair cells and the sensory arbors (27). In control neuromasts, the sensory axons
144 approached, arborized, and consolidated around the bases of clustered hair cells (Figure 2B).
145 Although the sensory axons approached the hair cells of *sema7a*$^{-/-}$ neuromasts, they displayed
146 aberrant arborization patterns with wayward projections that extended transversely to the organ
147 (Figure 2C). To quantitatively analyze the arborization morphology, we traced the sensory
148 arbors in three dimensions to generate skeletonized network traces that depict–as
149 pseudocolored trajectories–the increase in arbor length from the point of arborization
150 (Figure 2D, E).

151 To visualize the hair cell clusters and associated arborization networks from multiple
152 neuromasts, we aligned images of hair cell clusters, registered them at their hair bundles, from
153 neuromasts at 2 dpf, 3 dpf, and 4 dpf (Figure 2—figure supplement 1E,F). Throughout

development, the arborization networks of control neuromasts largely remained within the contours of the hair cell clusters; the few that reached farther nonetheless lingered nearby (Figure 2F; Figure 2—figure supplement 1G,I). This result suggests that an attractive cue retained the axons near the sensory organ. In *sema7a*$^{-/-}$ neuromasts, however the neuronal arbors failed to consolidate within the boundaries of hair cell clusters and extended far beyond them (Figure 2G; Figure 2—figure supplement 1H,J; Video 4).

We quantified the distribution of the sensory arbors around the center of the combined hair cell clusters. For both the control and the *sema7a*$^{-/-}$ neuromasts, the arbor densities peaked proximal to the boundaries of the hair cell clusters. Beyond the cluster boundaries, in control neuromasts at 2 dpf, 3 dpf, and 4 dpf the arbor densities fell sharply at respectively 31.7 μm, 36.6 μm, and 32.7 μm from the center. In *sema7a*$^{-/-}$ neuromasts of the same ages, the sensory arbors extended respectively 38.5 μm, 51.4 μm, and 56.6 μm from the center (Figure 2H; Figure 2—figure supplement 1K,L; Figure 2—figure supplement 2A). Furthermore, we quantified the degree of contact of the sensory arbors to their hair cell clusters in individual neuromasts from both control and *sema7a*$^{-/-}$ mutants. In control neuromasts, the degree of contact was 83 ± 1 % (mean ± SEM) at 2 dpf and 84 ± 1 % at 3 dpf, but significantly increased to 90 ± 1 % at 4 dpf (Figure 2I; Figure 2—figure supplement 2B). This observation indicates that the sensory arbors reinforce their association to the hair cell clusters as neuromasts develop. However, in *sema7a*$^{-/-}$ neuromasts such contact was significantly reduced. Only 69 ± 4 % of sensory arbors at 2 dpf were closely associated with the corresponding hair cell clusters, a value that remained at 67 ± 2 % at both 3 dpf and 4 dpf (Figure 2I). These findings signify that, with simultaneous disruption of both signaling modalities of Sema7A, the organ fails to restrict the localization of sensory arbors and has significantly diminished contact with them.

Sema7A patterns the arborization network's topology. Accurate spatial arrangement of the neuronal projections around hair cells is essential for proper retrieval and transmission of sensory information. Mutations that perturb proper assembly of sensory neuronal microcircuits lead to hearing impairment (28). Quantitative insight into the wiring pattern is therefore essential

182 to identify systematic aberrations in the microcircuit arising from genetic deficits. The three-
183 dimensional skeletonized network traces allowed us to accurately delineate the microcircuit
184 topology across individuals, developmental stages, and genotypes from living animals (Figure
185 2D, E). To quantitatively analyze the arbor network, we defined five topological attributes: (1)
186 nodes, denoted as junctions where arbors branch, converge, or cross; (2) loops, comprising
187 minimal arbor cycles forming topological holes; (3) bare terminals, defined as arbors with free
188 ends; (4) the node degree, calculated as the number of first-neighbor nodes incident to a node;
189 and (5) the arbor curvature, measured as the total curvature of a bare terminal (Figure 3A). We
190 quantified these attributes to accurately determine how the circuit topology is established
191 during maturation of the sensory organ in control larvae and how it is impacted by *sema7a*
192 deficit.

193 To determine how internode connectivity is distributed across networks, we quantified
194 the distribution of node degrees along the relative height of the hair cell cluster across
195 individuals, developmental stages, and genotypes. As for most other real-world networks (29),
196 we observed a highly skewed node-degree distribution: the majority of nodes had low node
197 degrees (three and four) and a small number of nodes—often acting as hubs, like the
198 arborization initiation point—had high node degrees (five to seven). The node degree varied
199 from three to seven in control larvae and three to six in *sema7a*$^{-/-}$ larvae. Across
200 developmental stages and genotypes, the high node degrees primarily occurred at the base
201 (region from 0 % to 10 % of the cluster height) of the hair cell cluster and acted as hubs for
202 the majority of branching events. Low node degrees primarily occurred along the basolateral
203 region (region from 10 % to 60 % of the cluster height) of the hair cell cluster. The apical region
204 (region from 60 % to 100 % of the cluster height) was sparsely populated with low node
205 degrees. The network's hierarchical organization along the organ's axis suggests that arbors
206 receive sensory inputs at multiple levels, allowing the network to carry out robust neural
207 computations. Even though nodes of low degree were most prevalent between genotypes
208 across developmental stages, their distribution along the relative organ axis became
209 significantly different at 4 dpf, with nodes in control larvae localized higher along the axis than

210 in *sema7a*$^{-/-}$ larvae (Figure 3A; Figure 3—figure supplement 1A-C; Table 1). These
211 observations indicate that Sema7A regulates both the spatial organization and node-degree
212 complexity of the sensory arbor network.

213 An average of 9.3 sensory axonal branches approach the hair cell cluster of a neuromast
214 (8). Pathfinding of sensory axons around the hair cell cluster results in the formation of axonal
215 fascicles that form numerous loops and bare terminals, which determine the microcircuit
216 topology (Figure 2B, D) (8). To optimally surround and contact the hair cell cluster, do the
217 sensory arbors prefer to adopt one topological feature over the other? To address this
218 question, we measured the correlation between the number of bare terminals and the number
219 of loops across individuals, developmental stages, and genotypes. In both 2 dpf and 3 dpf
220 larvae, the distributions remained highly scattered across individuals and genotypes.
221 However, by 4 dpf in the control larvae the arbor network contained either a high number of
222 loops with a low number of bare terminals or a high number of bare terminals with a low
223 number of loops. This result suggests that the stereotypical circuit topology observed in the
224 mature organ may emerge through transition of individual arbors from forming bare terminals
225 to forming closed loops encircling topological holes. That we did not observe a similar
226 transition in *sema7a*$^{-/-}$ neuromasts of the same age suggests that Sema7A may direct the
227 switch between these two distinct topological features (Figure 3B; Figure 3—figure
228 supplement 1D, E; Table 1).

229 Measurement of the contour length of both bare terminals and loops additionally
230 revealed that across developmental stages in control larvae the sensory arbors followed a
231 three-step process to choose the appropriate topological feature: arbors shorter than 10 μm
232 always formed bare terminals; arbors between 10 μm and 30 μm began to switch between
233 features, with arbors longer than 20 μm strongly preferring to form loops; and arbors longer
234 than 30 μm always formed loops. These results imply that the switch between bare terminals
235 and loops is partly dependent on the length of the arbors. However, this characteristic
236 topological preference was significantly perturbed in the *sema7a*$^{-/-}$ larvae across
237 developmental stages, as many of the sensory arbors longer than 30 μm remained as bare

238 terminals (Figure 3C; Figure 3—figure supplement 1F,G; Table 1). Furthermore, in 4 dpf
239 control neuromasts the majority of the loops contained four nodes and utilized 30-40 μm of
240 arbors to form closed cycles. These conserved topological attributes were significantly
241 perturbed in the *sema7a*$^{-/-}$ larvae of same age (Figure 3D, E; Figure 3—figure supplement
242 2A-D; Table 1). These findings indicate that Sema7A tightly monitors the sensory arbor loop
243 formation, including the preferred loop length and number of nodes per loop, to properly
244 surround and contact the hair cell cluster.

245 As observed previously, bare terminals in control neuromasts project transverse to the
246 organ and linger nearby, often curving back to form new loops and contact the hair cell cluster
247 (Figure 2D,F). To analyze the propensity of the bare terminals to curl backward, we measured
248 their total curvatures, defined as the sum of the curvature at each point along the length of an
249 arbor. Henceforth, we address the total curvature as the curvature of a bare terminal. We
250 classified the bare terminals in two categories: high-curvature arbors with curled morphology
251 and curvature greater than $\pi/6$ (30 degrees); and low-curvature arbors with linear morphology
252 and curvature less than $\pi/6$. In control neuromasts 44.8 % of arbors had low curvature
253 compared to 56.4 % in *sema7a*$^{-/-}$ neuromasts at 4 dpf. Concomitantly, 55.2 % of arbors had
254 high curvature in control neuromasts compared to 43.6 % in *sema7a*$^{-/-}$ neuromasts at 4 dpf
255 (Figure 3F; Figure 3—figure supplement 2E, F; Table 1). These observations further confirm
256 our hypothesis that a Sema7A-mediated attractive cue is involved in orienting bare neural
257 arbors toward the hair cell cluster to potentially form loops.

258 In summary, we propose that Sema7A mediates four key aspects of the topology of the
259 arborization network: (1) the node degree complexity along the organ's axis; (2) the transition
260 of arbors from bare terminals to loops; (3) the preference for forming loops containing four
261 nodes with 30-40 μm of arbors; and (4) the preference of bare terminals to adopt higher
262 curvature.

263 **Sema7A^{sec} is a sufficient chemoattractive cue for sensory axon guidance**. Because
264 genetic inactivation of the *sema7a* gene disrupts both signaling modalities of the cognate
265 protein, we could not assess the specific activity of the Sema7A^{sec} diffusive cue in guiding

266 lateral-line sensory axons. To independently verify the potential role of that isoform, we
267 therefore expressed the secreted variant ectopically and investigated the resultant arborization
268 patterns.

269 Analysis of the microcircuit connectivity of the neuromasts has demonstrated bare
270 sensory-axonal terminals in the perisynaptic compartments, where they do not contact the hair
271 cell membrane (8). We speculate that these bare terminals are attracted by a Sema7A^{sec}
272 diffusive cue. To test this hypothesis, we ectopically expressed Sema7A^{sec} protein tagged with
273 the fluorophore mKate2, then analyzed its effect on the morphology of sensory arbors.
274 Fertilized one-cell embryos were injected with the *hsp70:sema7a^{sec}-mKate2* plasmid and
275 raised to 3 dpf. Larvae expressing the transgenesis marker—the lens-specific red fluorescent
276 protein mCherry—were heat-shocked, incubated to allow expression, and subsequently
277 mounted for live imaging. In these larvae, a random mosaic of cells—often embryonic muscle
278 progenitors in the dermomyotome or mature myofibers—expressed the exogenous
279 Sema7A^{sec}-mKate2 protein. We selected only those neuromasts in which a single mosaic
280 ectopic integration had occurred near the network of sensory arbors (Figure 4A,B). In all 22
281 such cases, we observed robust axonal projections from the sensory arbor network toward the
282 ectopically expressing Sema7A^{sec} cells. When the exogenous *sema7a^{sec}* integration occurred
283 in embryonic muscle progenitor cells, which reside in a superficial layer external to the muscle
284 fibers and adjacent to the larval skin (30), the projections were able to form direct contacts with
285 them (Figure 4C; Videos 5,6). But more often, when mature myofibers expressed the
286 exogenous Sema7A^{sec} deep in the myotome, the axonal projections approached those targets
287 but failed to contact them (Figure 4D, Videos 7,8). This behavior likely arose because other
288 components in the myotomal niche—including the fibrous epimysium, other myofibers,
289 myoblasts, and immature myotubes whose surroundings are permeable to diverse diffusive
290 cues (31)—physically obstructed direct interaction of the extended neurites with the ectopically
291 expressing myofibers. All 18 of the injected but not heat-shocked control larvae did not express
292 ectopic Sema7A^{sec}, and we did not observe aberrant projections from the sensory arbor
293 network (Figure 4E).

294 To measure the accuracy of the extended axonal projections in finding the ectopic
295 Sema7A^{sec} source, we defined three parameters: (1) the source path, denoted as the linear
296 distance from the point of arborization to the boundary of an ectopically expressing Sema7A^{sec}
297 cell; (2) the projection path, representing the linear distance from the point of arborization to
298 the terminus of the extended projection; and (3) the projection proximity, calculated as the
299 linear distance from the terminus of the extended axonal projection to the nearest boundary of
300 the ectopically expressing Sema7A^{sec} cell (Figure 4B). We quantified these parameters from
301 18 of the 22 mosaic integration events; in the remainder the extended axonal projections–
302 although following the ectopic source–reentered the posterior lateral-line nerve so that
303 identification of the axon terminals was not possible (Figure 4—figure supplement 1A-A";
304 Video 9). When we plotted the projection path length against the source-path length, we
305 observed a nearly perfect correlation (Figure 4F). This result signifies that irrespective of the
306 location of the ectopic source–whether proximal or distal to the sensory arbor network–the
307 Sema7A^{sec} cue sufficed to attract axonal terminals from the sensory arbor. Furthermore, the
308 low average projection-proximity length of $3.5 \pm 0.7\ \mu$m (mean ± SEM) indicated that the
309 extended projection terminals remained either in contact (8 of 18) or in the vicinity (10 of 18) of
310 the ectopic Sema7A^{sec} sources (Figure 4G). These observations together demonstrate that the
311 Sema7A^{sec} diffusive cue is sufficient to provide neural guidance *in vivo*.

312 As the posterior lateral-line ganglion matures, newly formed neurons extend their axonal
313 growth cones along the posterior lateral-line nerve to reach the neuromasts (32). We wondered
314 whether the axonal projections that had yet to be associated with a neuromast could also
315 respond to an ectopic source of Sema7A^{sec}. Indeed, on seven occasions in which *sema7a^{sec}*
316 integration had occurred between two neuromasts, we detected neurite extensions from the
317 posterior lateral-line nerve to the ectopic Sema7A^{sec} sources (Figure 4H; Figure 4—figure
318 supplement 1B-B", Videos 10-12). Live time-lapse video microscopy further revealed dynamic
319 association between the extending neurites and the ectopic Sema7A^{sec} sources. Long and thin
320 along their entire extents, the neurites were highly motile, extending and retracting rapidly near
321 the Sema7A^{sec} expressing cells. Many neurites maintained their contact with the ectopic

322 sources of Sema7A^{sec} from one hour to almost eight hours (Figure 4I,J; Figure 4—figure
323 supplement 2A, Videos 13-16). The responsiveness of the posterior lateral-line axons to
324 Sema7A^{sec} might therefore be an intrinsic property of the neurons that does not require the
325 neuromast microenvironment.

326 **Sema7A-GPI fails to impart sensory axon guidance from a distance**. We speculate that
327 the GPI-anchored transcript variant of the *sema7a* gene can function only through contact-
328 dependent pathways. To test this hypothesis, we expressed the Sema7A-GPI ectopically and
329 investigated the resultant arborization patterns of the sensory axons. Fertilized one-cell
330 embryos were injected with the *hsp70:sema7a-GPI-2A-mCherry* plasmid and raised to 3 dpf.
331 Larvae expressing the transgenesis marker—the lens-specific green fluorescent protein
332 (GFP)—were heat-shocked, incubated to allow expression, and subsequently mounted for live
333 imaging (Figure 5A). In these larvae, a few mature myofibers expressed the exogenous
334 Sema7A-GPI protein. We selected only those neuromasts in which an ectopic integration had
335 occurred near the network of sensory arbors. In all 15 such cases, no sensory axon left the
336 arbor network to approach the ectopic Sema7A-GPI sources. In all 17 of the uninjected and
337 heat-shocked control larvae, the sensory arbor network did not show any perturbation
338 (Figure 5B-C, Videos 17-19). These data suggest that the Sema7A-GPI, unlike its secreted
339 counterpart, functions at the surfaces of the expressing cells.

340 **Sema7A deficiency impacts synaptic assembly.** Contact stabilization between an axon and
341 its target cell is essential for synapse formation (33). Neural GPI-anchored proteins can act as
342 regulators of various synaptic-adhesion pathways (34). In the mouse olfactory system, GPI-
343 anchored Sema7A is enriched in olfactory sensory axons and mediates sustained interaction
344 with the dendrites of mitral and tufted cells in the olfactory bulb to establish synapses (15). In
345 the developing mouse brain–particularly in Purkinje cells–GPI-anchored Sema7A instead
346 regulates the elimination of synapses onto climbing fibers (35). The role of anchored Sema7A
347 in regulating synaptic architecture can thus vary according to the cell type and developmental
348 stage. Our demonstration that Sema7A is necessary to consolidate the contact between

349 sensory axons and hair cells during neuromast development suggests a possible role in
350 regulating synaptic structure.

351 Proper synaptogenesis requires the correct spatial organization of the presynaptic and
352 postsynaptic apparatus at the apposition of two cells. At the interface between hair cells and
353 sensory axons, the synaptic network involves two scaffolding proteins in particular: ribeye, a
354 major constituent of the presynaptic ribbons (36), and membrane-associated guanylate kinase
355 (MAGUK), a conserved group of proteins that organize postsynaptic densities (37). Utilizing
356 these scaffolding proteins as markers, we investigated the impact of the *sema7a*$^{-/-}$ mutation on
357 synapse formation. To analyze the distribution of presynaptic densities–immunolabeled with
358 an antibody against the ribeye-associated presynaptic constituent C-terminal binding protein
359 (CTBP) (36)–we counted the number and measured the area of CTBP punctae from multiple
360 neuromasts at several stages of neuromast development (Figure 6A,B). The CTBP punctae in
361 each hair cell ranged from zero to seven across developmental stages. In the zebrafish's
362 posterior lateral line, the formation of presynaptic ribbons is an intrinsic property of the hair cells
363 that does not require contact with lateral-line sensory axons. However, sustained contact with
364 the sensory axon influences the maintenance and stability of ribbons (38). As neuromasts
365 matured from 2 dpf to 4 dpf, we identified similar distribution patterns with a characteristic
366 increase in the number of CTBP punctae in both control and *sema7a*$^{-/-}$ larvae (Figure 6C,D).
367 This result implies that the formation of new presynaptic ribbons is not perturbed in the mutants,
368 even though there are on average fewer CTBP punctae (Figure 6—figure supplement 1A-C).
369 Measurement of the areas of CTBP punctae also showed similar distributions in both
370 genotypes (Figure 6E,F) but the average area of presynaptic densities was reduced in the
371 mutants (Figure 6—figure supplement 1D-F, Figure 6—figure supplement 2). Because GPI-
372 anchored Sema7A lacks a cytosolic domain, it is unlikely that Sema7A signaling directly
373 induces the formation of presynaptic ribbons. We propose that the decrease in average number
374 and area of CTBP punctae likely reflects decreased stability of the presynaptic ribbons owing
375 to lack of contact between the sensory axons and the hair cells.

376 Our analysis of the skeletonized network traces of the sensory arbor network identified
377 distinct topological features that are resultant of collective assemblies of each sensory axon.
378 Because postsynaptic aggregates are organized at the sensory axons, we wondered whether
379 they are associated with a specific topological feature of the network. To identify the distribution
380 of the postsynaptic aggregates along the arbor network, we utilized the transgenic animal
381 *TgBAC(neurod1:EGFP)* that labeled the sensory axons of the posterior lateral line in green
382 fluorescence protein (GFP), and marked the postsynaptic aggregates through immunostaining
383 with a pan-MAGUK antibody (Figure 6G). We generated skeletonized network traces of the
384 arbor network and determined the three-dimensional spatial locations of the MAGUK punctae
385 (Figure 6—figure supplement 2). Comparison of the topological features of the network and the
386 spatial locations of the MAGUK punctae revealed that the postsynaptic densities occur more
387 extensively on the loops than on the bare terminals (Figure 6G,H). We measured 567 MAGUK
388 punctae from 16 sensory arbor networks, where 531 punctae were located on the loops and
389 only 36 punctae on the bare terminals. Furthermore, the MAGUK punctae predominantly
390 aggregate near the node and their density sharply diminishes moving farther from the node
391 (Figure 6I, Figure 6—figure supplement 2). These observations suggest that the distribution of
392 the postsynaptic aggregates is closely associated with the topological attributes of the sensory
393 circuit. Because in the *sema7a*$^{-/-}$ mutants the arbor networks have significantly lower number
394 of loops and nodes, and more bare terminals, we hypothesize that in the mutants the
395 occurrence of postsynaptic aggregates is perturbed. Moreover, Sema7A-GPI-mediated
396 juxtracrine signaling onto the apposed axonal membrane is essential to induce postsynaptic
397 assembly (15).

398 To characterize the impact of *sema7a* mutation on the formation of postsynaptic
399 aggregates, we counted the number and measured the area of MAGUK punctae from multiple
400 neuromasts at several stages of neuromast development (Figure 6J,K). At 4 dpf, 68.3 % of the
401 hair cells in the control neuromasts were associated with at least one MAGUK punctum. In the
402 *sema7a*$^{-/-}$ mutant this value fell to 37.5 % (Figure 6L,M). The average number of MAGUK
403 punctae also declined in the mutants (Figure 6—figure supplement 1G-I). As control

404 neuromasts matured from 2 dpf to 4 dpf, the MAGUK punctae showed a shift toward smaller
405 sizes, suggesting that the postsynaptic structure fragmented into smaller entities as observed
406 in other excitatory synapses (40). At 4 dpf, 77.5 % of the hair cells in the control neuromasts
407 had postsynaptic densities with areas between 0.10 μm^2 and 0.40 μm^2. In the *sema7a*$^{-/-}$ mutant
408 the corresponding value was only 42.5 % (Figure 6N,O). The average area of MAGUK punctae
409 was also reduced in the mutants compared to the controls (Figure 6—figure supplement 1J-L,
410 Figure 6—figure supplement 2**).** We speculate that the abnormalities in the postsynaptic
411 structure of the *sema7a*$^{-/-}$ mutants arose from reduced contact between the hair cells and the
412 sensory axons and perturbed topological attributes of the sensory circuit or from the lack of
413 Sema7A-GPI-mediated juxtracrine signaling onto the apposed neurite terminals (15).

414 **Discussion**

415 The specification of neural circuitry requires precise control of the guidance cues that direct
416 and restrict neural arbors at their target fields and facilitate synapse formation. In the lateral-
417 line neuromast of the zebrafish, we have identified Sema7A as an essential cue that regulates
418 the interaction between hair cells and sensory axons. We have discovered dual modes of
419 Sema7A function *in vivo*: the chemoattractive diffusible form is sufficient to guide the sensory
420 arbors toward their target, whereas the membrane-attached form likely participates in sculpting
421 accurate neural circuitry to facilitate contact-mediated formation and maintenance of synapses.
422 Our results suggest a potential mechanism for hair cell innervation in which a local Sema7A^{sec}
423 diffusive cue likely consolidates the sensory arbors at the hair cell cluster and the membrane-
424 anchored Sema7A-GPI molecule guides microcircuit topology and synapse assembly.

425 The role of Sema7A in regulating diverse topological features of the arborization network
426 suggests that microcircuits of control and *sema7a*$^{-/-}$ neuromasts have important functional
427 differences. Loss of Sema7A disrupts the hierarchical organization of the node-degree
428 distribution along the organ's axis, as well as the preference towards forming loops containing
429 four nodes with 30-40 μm of arbors. What benefit does the network gain from surrounding the
430 hair cell cluster with closed loops instead of bare terminals? The network may actively form

431 loops to contribute to the neuromast's overall structure and function, or else emerge as a
432 consequence of the arbors navigating the intervening spaces between the hair cells and
433 support cells. The preferential localization of the postsynaptic aggregates in the loops and an
434 enrichment near the nodes of the arbor network suggest that the precise patterning of the
435 network—with characteristic looping behaviors—is not merely a byproduct of neuromast
436 architecture, but may contribute to the network's ability to gather sensory inputs through
437 properly placed postsynaptic aggregates and to faithfully transmit sensory information to higher
438 processing centers in the hindbrain (7). Further studies are necessary to elucidate the potential
439 role of these topological features in regulating the distribution of synaptic bodies and optimizing
440 robust neural transmission in the lateral-line microcircuit.

441 Recent studies have begun to dissect the molecular mechanisms of semaphorin
442 signaling in axonal navigation. In explants derived from the murine olfactory bulb, Sema7A
443 interacts directly with integrinβ1 to trigger downstream signaling effectors involving focal
444 adhesion kinase and mitogen-activated protein kinases, which are critical regulators of the
445 cytoskeletal network during axonal pathfinding (4,41). Moreover, the interaction between
446 Sema7A and its receptor plexinC1 activates the rac1-cdc42-PAK pathway, which alters the
447 actin network to promote axonal guidance and synapse formation (15,42). We speculate that
448 lateral-line sensory axons utilize similar mechanisms to sense and respond to Sema7A in the
449 establishment of microcircuits with hair cells.

450 During early development of the posterior lateral line, the growth cones of sensory axons
451 intimately associate with the prosensory primordium that deposits neuromasts along the lateral
452 surface of the larva (43,44). The growth of the sensory fibers with the primordium is regulated
453 by diverse neurotrophic factors expressed in the primordium (45,46). Impairing brain-derived
454 or glial cell line-derived neurotrophic factors and their receptors perturbs directed axonal
455 motility and innervation of hair cells (45,46). Lateral-line hair cells are particularly enriched in
456 brain-derived neurotrophic factor (47) and other chemotropic cues (Figure 7). Because the
457 sensory axons of *sema7a*$^{-/-}$ mutants reliably branch from the lateral-line nerve to reach hair cell
458 clusters, these chemoattractive factors might compensate in part for the absence of Sema7A

459 function. Although sensory axons are strict selectors of hair cell polarity and form synapses
460 accordingly (5), diverse chemoattractant cues including Sema7A occur uniformly between hair
461 cell polarities (47). It seems likely that unbiased attractive signals bring sensory arbors toward
462 hair cells, after which polarity-specific molecules on hair cell surfaces dictate the final
463 association between axonal terminal and hair cells. Notch-delta signaling and its downstream
464 effectors regulate hair cell polarity and the innervation pattern (6,8,27). It would be interesting
465 to determine whether Notch-mediated polarity signatures on the hair cell's surface can refine
466 the neuromast neural circuitry.

467 **Materials and Methods**

468 **Zebrafish strains and husband**ry. Experiments were performed on 1.5-4 dpf zebrafish larvae
469 in accordance with the standards of Rockefeller University's Institutional Animal Care and Use
470 Committee. Naturally spawned and fertilized eggs were collected, cleaned, staged, and
471 maintained at 28.5 ºC in system-water with 1 µg/mL methylene blue. Wild-type AB and
472 heterozygous mutant *semaphorin7a*^{sa24691} zebrafish were obtained from the Zebrafish
473 International Resource Center. In addition, the following transgenic zebrafish lines were used:
474 *Tg(myo6b:actb1-EGFP)* (48), *Tg(neurod1:tdTomato)* (27), *Tg(cldnb:LY-mScarlet)* (26), and
475 *TgBAC(neurod1:EGFP)* (39).

476 **Embryo dissociation and flow cytometry**. Immediately before dissection, 4-day-old
477 *Tg(myo6b:actb1-EGFP)* and wild-type larvae were anesthetized in 600 µM 3-aminobenzoic
478 acid ethyl ester methanesulfonate in system water with 1 µg/mL methylene blue. The anterior
479 half of each larva was removed with a fine surgical blade. We used approximately 400 GFP-
480 positive and 50 GFP-negative larvae, the latter for controls of the gating procedure.
481 Dissociation of the tails were performed using a protocol (22) with minor modification; detailed
482 protocol is available upon request. The resuspended cells were incubated for 5 min on ice and
483 sorted with an influx cell sorter (BD Biosciences, San Jose, CA, USA) with an 85 µm nozzle at
484 20 psi and 1X DPBS (Sigma-Aldrich, St Louis, USA). Laser excitation was conducted at

485 561 nm and 488 nm. Distinct populations of GFP-positive hair cells were isolated based on
486 forward scattering, lateral scattering, and the intensity of GFP fluorescence.

487 **RNA extraction and cDNA library preparation**. Sorted cells were collected in a lysis-buffer
488 solution supplemented with β-mercaptoethanol and RNA extraction was performed
489 immediately using a standard protocol (RNeasy Plus Micro Kit; Qiagen). The yield and quality
490 of the product were measured with a bioanalyzer (Agilent 2100). Only samples with an RNA
491 integrity score (RIN) greater than 8.0 were selected for the preparation of cDNA libraries using
492 iScript cDNA Synthesis Kit (BioRad). One nanogram of total RNA was amplified to several
493 micrograms of cDNA.

494 **Reverse transcription-polymerase chain reactions (RT-PCR)**. The *sema7a* gene
495 expresses two transcript variants: variant 1, *sema7a-GPI* anchored, NM_001328508.1; and
496 variant 2, *sema7a*^{sec} secreted, NM_001114885.2. The variant 2 lacks several C-terminal
497 exons, and its 3'-terminal exon extends past a splice site that is used in variant 1. The encoded
498 variant 2 has a shorter and distinct C-terminus than variant 1. To individually identity these
499 transcripts, each of them was PCR amplified from the cDNA library using the following primers:
500 For variant 1, sema7aF= 5´-GGTTTTTCTGAGGCCATTCC-3´, sema7aR1=
501 5´-GGCACTCGTGACAAATGCTA-3´; and for variant 2, sema7aF=
502 5´-GGTTTTTCTGAGGCCATTCC-3´, sema7aR2= 5´-TGTGGAGAAAGTCACAAAGCA-3´. To
503 detect *pvalb8* transcript we used the following primers: pvalb8F=
504 5´-ATGTCTCTCACATCTATCCT-3´ and pvalb8R= 5´-TCAGGACAGCACCATCGCCT-3´. To
505 detect *s100t* transcript we used the following primers: s100tF=
506 5´-ATGCAGCTGATGATCCAGAC-3´ and s100tR= 5´-CTATTTCTTGTCATCCTTCT-3´.

507 **Immunofluorescence microscopy.** For the immunofluorescence labeling of wholemounted
508 wild-type control and *sema7a*$^{-/-}$ larvae, 1.5-4 dpf larvae were fixed overnight at 4 °C in 4 %
509 formaldehyde in phosphate-buffered saline solution (PBS) with 1 % Tween-20 (1 % PBST).
510 Larvae were washed four times with 1 % PBST for 15 min each, then placed for 2 hr in blocking
511 solution containing PBS, 2 % normal donkey serum (NDS), 0.5 % Tween-20, and 1 % BSA.

512 Primary antibodies were diluted in fresh blocking solution and incubated with the specimens
513 overnight at 4 °C. The primary antibodies were goat anti-Sema7A (1:200; AF1835, R&D
514 Systems) (Figure 1—figure supplement 4) (14), rabbit anti-myosin VI (1:200; Proteus 25-6791),
515 murine anti-GM130 (1:200; 610822, BD Transduction Laboratories), murine anti-CTBP (1:200;
516 B-3, SC-55502, Santa Cruz Biotech), and rabbit anti-mCherry (1:200; GTX128508, GeneTex).
517 Larvae were washed four times with 0.1% PBST for 15 min each. Alexa Fluor-conjugated
518 secondary antibodies (Invitrogen, Molecular Probes) applied overnight at 1:200 dilutions in
519 0.2 % PBST included anti-rabbit (488 nm), anti-goat (555 nm), and anti-mouse (647 nm).
520 Larvae were then washed four times in 0.2 % PBST for 15 min each and stored at 4 °C in
521 VectaShield (Vector Laboratories).

522 For the immunofluorescence labeling of postsynaptic density in wholemounted wild-type
523 control and *sema7a*$^{-/-}$ larvae, 2-4 dpf larvae were fixed with 4 % formaldehyde in PBS for
524 4.5-6 hr at 4 °C. Larvae were washed five times with 0.01 % PBST for 5 min each and then
525 rinsed in distilled water for 5 min. The larvae were permeabilized with ice-cold acetone at -20 °C
526 for 5 min. They were rinsed in distilled water for 5 min, washed five times with 0.01 % PBST
527 for 5 min each, and blocked overnight with PBS buffer containing 2 % goat serum and 1 %
528 BSA. Murine anti-pan-MAGUK antibody (1:500; IgG1 NeuroMab, K28.86, 75-029 and
529 MABN72, Millipore) was diluted in PBS containing 1 % BSA, added to the larvae, and incubated
530 for 3 hr at room temperature. Larvae were washed five times for 5 min each with 0.01 % PBST.
531 Alexa Fluor 555-conjugated anti-mouse secondary antibody (1:1000) diluted in PBS containing
532 1 % BSA was added to the larvae and incubated for 2 hr at room temperature. Larvae were
533 washed five times with 0.01 % PBST for 5 min each, rinsed in distilled water for 5 min, and
534 stored at 4 °C in VectaShield (Vector Laboratories).

535 Posterior segments of fixed larvae were mounted on a glass slide and imaged on an
536 Olympus IX81 microscope with a microlens-based, super-resolution confocal microscope
537 (VT-iSIM, VisiTech international) under 60X and 100X, silicone-oil objective lenses of
538 numerical apertures 1.30 and 1.35, respectively. Static images at successive focal depths were
539 captured at 200 nm intervals and deconvolved with the Microvolution software in ImageJ.

540 **Measurement of Sema7A and td-Tomato$^+$ sensory arbor intensities.** The average Sema7A
541 fluorescence intensities of the hair cells from 1.5 dpf, 2 dpf, 3 dpf, and 4 dpf neuromasts were
542 measured by determining the mean gray level within each hair cell labeled by actin-GFP
543 expression. The intensity distribution of Sema7A protein across the basal cell membrane was
544 measured using the line profile tool in ImageJ (Figure 1—figure supplement 2F-H). The lines
545 were drawn with 1 µm length, starting from the inside of the hair cell to the outside. For each
546 hair cell membrane, the intensity values were scaled from 0 to 1 arbitrary units. The intensity
547 distribution of Sema7A protein along the apicobasal axis of the hair cell was measured using
548 the line profile tool in ImageJ (Figure 1—figure supplement 2I). Because hair cell lengths
549 differed among samples, lines were drawn with 2 µm widths and varying lengths of 6-8 µm. For
550 each hair cell, apicobasal length was scaled from 0 to 100 arbitrary units and the intensity
551 values from 0 to 1 arbitrary units. The average Sema7A and td-Tomato$^+$ sensory arbor
552 fluorescence intensities at the hair cell bases from 2 dpf, 3 dpf, and 4 dpf neuromasts were
553 measured by determining the mean gray level within each hair cell basal area, denoted by the
554 region underneath the hair cell nucleus (Figure 1—figure supplement 3A-E).

555 **Genotyping of mutant fish.** The *semaphorin7a^{sa24691}* allele harbors an A-to-T point mutation
556 in the seventh exon of the *semaphorin7a* gene, which creates a premature stop codon (Figure
557 2—figure supplement 1A). Genomic DNA was isolated from the tail fins of adult
558 *semaphorin7a^{sa24691}* (*sema7a^{sa91}*) heterozygous mutant zebrafish. The mutant locus in the
559 genome was PCR amplified using the following primers: sema7a^{sa91}F:
560 5´-AAAGCTGGAAAGCGAATCAA-3´ and sema7a^{sa91}R: 5´-ATATCCAAGGATCCGCCTCT-3´.
561 The 734-base pair amplicons were sequenced, and heterozygous adults were propagated.

562 **Lipophilic styryl fluophore labeling of hair cells.** Freely swimming 4 dpf control and
563 *sema7a$^{-/-}$* larvae were exposed to the styryl fluorophore FM4-64
564 (N-(3-triethylammoniumpropyl)-4-(6-(4-(diethylamino) phenyl) hexatrienyl) pyridinium
565 dibromide, ThermoFischer Scientific) at 5 μM for 30 s, then rinsed three times in fresh embryo
566 water and immediately mounted in low-melting-point agarose for live imaging.

567 **Transient transgenesis with the hsp70l:sema7a^{sec}-mKate2 construct.** The pDNR-LIB
568 plasmid containing the *sema7a^{sec}* coding sequence was purchased from horizon (7140389,
569 Perkin-Elmer). The coding sequence was PCR amplified using the following primers:
570 sema7a^{sec}F:
571 5´-GGGGACAAGTTTGTACAAAAAAGCAGGCTTGATGATTCGACATTATTCT-3´ and
572 sema7a^{sec}R:
573 5´-GGGGACCACTTTGTACAAGAAAGCTGGGTG*CTT*TGTGGAGAAAGTCACAAAGCA-3´.
574 The italicized nucleotides denote the mutated stop codon. The amplicon was then cloned into
575 the pDONR221 vector by BP recombination to generate the middle entry pME-sema7a^{sec}
576 vector. To generate the hsp70:sema7a^{sec}-mKate2 construct, gateway cloning was performed
577 by combining the plasmids p5E-hsp70 (49), pME-sema7a^{sec}, p3E-mKate2-myc no-pA
578 (Addgene, 80812), and pDESTtol2pACrymCherry (Addgene, 64023) with LR Clonase II Plus
579 (Invitrogen). Verified constructs (25 ng/µl plasmid DNA) were injected with Tol2 Transposase
580 mRNA (approximately 25 ng/µl) into one-cell embryos. The transiently transgenic larvae—
581 identified by the expression of red fluorescent protein (mCherry) in their lenses—were raised
582 till 3 dpf, heat-shocked in a water bath at 37 ºC for 1 hr, incubated at 28 ºC for 1 hr to allow
583 expression, and subsequently mounted for live imaging.

584 **Transient transgenesis with the hsp70l:sema7a-GPI-2A-mCherry construct.** The *sema7a-*
585 *GPI* coding sequence without the stop codon (*sema7a-GPI$^{no\text{-}stop}$*) was synthesized using
586 gBlocks HiFi Gene Fragments (Integrated DNA Technologies). The *sema7a-GPI$^{no\text{-}stop}$* coding
587 sequence was then cloned into the pDONR221 vector by BP recombination to generate the
588 middle entry pME-sema7a-GPI$^{no\text{-}stop}$ vector, henceforth denoted as pME-sema7a-GPI. To
589 generate the hsp70:sema7a-GPI-2A-mCherry construct, gateway cloning was performed by
590 combining the plasmids p5E-hsp70 (49), pME-sema7a-GPI, p3E-2A-mcherrypA (Addgene,
591 26031), and pDESTtol2pACryGFP (Addgene, 64022) with LR Clonase II Plus (Invitrogen).
592 Verified constructs (25 ng/µl plasmid DNA) were injected with Tol2 Transposase mRNA
593 (approximately 25 ng/µl) into one-cell embryos. The transiently transgenic larvae—identified
594 by the expression of green fluorescent protein (GFP) in their lenses—were raised till 3 dpf,

595 heat-shocked in a water bath at 37 ºC for 1 hr, incubated at 28 ºC for 1 hr to allow expression,
596 and subsequently mounted for live imaging.

597 **Microscopy and volumetric rendering of living neuronal arbors and cells.** Living larvae
598 were dechorionated, anaesthetized in 600 µM 3-aminobenzoic acid ethyl ester
599 methanesulfonate in system-water with 1 µg/mL methylene blue, and mounted in 1 % low-
600 melting-point agarose on a glass-bottom MetTek dish at specific stages. The larvae were
601 maintained at 28 °C during imaging in a temperature-controlled stage top chamber (OKO Lab
602 UNO-T). Static images at successive focal depths were captured at 200 nm intervals and
603 deconvolved with Microvolution software in ImageJ (NIH). For time-lapse video microscopy,
604 the ectopic *sema7a*^{sec} integration sites were imaged at intervals of 5 min as Z-stacks acquired
605 with 1.0 µm steps with laser excitation at 488 nm and 561 nm under a 60X, silicone-oil objective
606 lens of numerical aperture 1.30. The three-dimensional datasets were processed and volume-
607 rendered with the surface evolver and filament-tracer tools in Imaris (Bitplane, Belfast, UK).
608 The Imaris workstation was provided by the Rockefeller University Bio-imaging Resource
609 Center.

610 **Generation of pseudocolored trajectories of the dwell times of sensory neurites at the**
611 **ectopic Sema7A^{sec} sources.** Fluorescent intensity values of the sensory neurites and the
612 ectopic Sema7A^{sec} sources were measured from the maximal-intensity projections at each time
613 during the time-lapse video microscopy. The intensity values were normalized and binarized
614 before summing across each timepoint for locations across the XY plane. The resulting
615 pseudocolored trajectories represent the dwell times of the neurites and the Sema7A^{sec} cells
616 through the 10 hr time-lapse video sequence.

617 **Generation of skeletonized networks.** The labeled sensory axons were traced in three
618 dimensions with ImageJ's semi-automated framework, SNT (50). Each trace depicts the
619 skeletonized form of the posterior lateral-line nerve, the posterior lateral-line branch, and the
620 point of arborization from which the sensory arbors radiate to contact the hair cells
621 (Figure 2D,E; Figure 2—figure supplement 2B. The three-dimensional pixels or voxels

622 obtained from the skeletonized sensory arbor traces were processed using custom code written
623 in Python for visual representation and quantitative analysis.

624 **Generation of combined hair cell clusters and the corresponding combined skeletonized**
625 **networks.** The hair cell clusters of neuromasts from each developmental stage were aligned
626 by the centers of their apices, which were identified by the hair bundles, and overlayed to
627 generate combined hair cell clusters (Figure 2—figure supplement 1E,F) using custom Python
628 code. The associated skeletonized sensory-arbor traces at each developmental stage were
629 aligned similarly using custom Python code. The details of the procedures are available upon
630 request and the corresponding code is available on GitHub.

631 **Quantification of sensory arbor distributions around hair cell clusters.** The region from
632 the center of the combined hair cell cluster to 60 µm in the post-cluster region was divided into
633 3600 concentric sections of equal area. Each section, as depicted with a distinct color shade,
634 had an area of π μm^2. Sensory arbor density was defined as Log_{10}[(Area occupied by the arbors
635 in each section)/ (Area of each section)]. The arbor density was then plotted as a histogram
636 against distance from the center of the combined hair cell cluster. Each bin of the histogram
637 represents an area of π μm^2 (Figure 2—figure supplement 2A). The histograms were finally
638 represented as density trace graphs with Kernel Density Estimation (KDE) in Python.

639 **Quantification of contact between sensory arbors and hair cell clusters.** For each hair cell
640 cluster, the voxels of the sensory arbor traces that were inside or within 0.5 μm—the average
641 neurite radius—of the cluster boundary were denoted as arbors in contact with their
642 corresponding hair cell cluster (Figure 2—figure supplement 2B). The percentage of arbors in
643 contact with each hair cell cluster was defined as: (Number of voxels that remained inside the
644 cluster boundary/Total number of voxels in the arbor) X 100. The data were analyzed through
645 an automated pipeline with custom Python code.

646 **Quantification of the sensory arborization network topology.** We developed a custom
647 Python script (snt_topology.py; available on GitHub) to convert the skeletonized sensory

arborization networks to network graphs (NetworkX, v3.1). We first used a custom ImageJ macro to convert SNT skeletons to csv files, then generated the network graph from the individual arbor paths. As noted previously, we defined five topological attributes: (1) nodes—junctions where arbors branch, converge, or cross; (2) loops—minimal arbor cycles forming topological holes; (3) bare terminals—arbors with free ends; (4) node degree—the number of first-neighbor nodes incident to a node; and (5) arbor curvature—the total curvature of a bare terminal (Figure 3A). To enumerate loops and quantify their lengths and node numbers, we computed the minimum cycle basis for each network graph. The relative organ height of each node in a graph was defined in 3D using Equation (1):

$$(\vec{u} \cdot \vec{v}) \,/\, \|\vec{v}\|^2 , \tag{1}$$

where $\vec{u}$ is the vector from the arborization initiation point to a node and $\vec{v}$ is the vector from the arborization initiation point to the hair cell cluster apex. The relative occurrence of nodes (Figure 3—figure supplement 1A-C) was normalized by both the number of hair cells per neuromast and the total number of neuromasts, for comparison across ages and genotypes. The relative number of bare terminals and loops (Figure 3B; Figure 3—figure supplement 1D, E) was normalized by the number of hair cells per neuromast and scaled between 0 and 1. The density was then normalized by the total number of neuromasts imaged for each developmental stage and genotype. For Figure 3C and Figure 3—figure supplement 1F and G, the normalized occurrence was computed as the number of arbors of a given length that formed either a bare terminal or a loop, divided by the total number of arbors of either feature of that length. Lastly, we defined bare terminals as having either high or low curvature (Figure 3F; Figure 3—figure supplement 2E,F) if their absolute total signed curvature [Equation (2)] in three dimensions was either higher or lower than $\pi/6$, respectively:

$$\left| \int \frac{dT}{ds} \cdot N(s)\, ds \right|, \tag{2}$$

where s is the arc-length parameter of the bare terminal, $T(s)$ is the unit tangent vector at each point along the arbor, $N(s)$ is the unit normal vector at each point, and the integral is evaluated

674 from the terminal's branching node to the arbor's tip. For a closed curve forming a full loop, this
675 value will equal 2π. In practice, we first fit B-splines (scipy.interpolate.splprep; SciPy, v1.10.1)
676 in 3D to the skeletons for each bare terminal before evaluating their derivatives
677 (scipy.interpolate.splev) and integrating (scipy.integrate.simpson) over their lengths.

678 **Quantification of aberrant sensory arborization in ectopic Sema7A^{sec} expression.** The
679 sensory arbor networks were traced in three dimensions with SNT. The surface of each of the
680 ectopically expressing Sema7A^{sec}-mKate2 cells was represented by a single point that was
681 closest to the terminal point of the guided neurite. Distances between two points were
682 calculated using standard mathematical operations.

683 **Quantification of presynaptic and postsynaptic assembly number and area.** Maximal-
684 intensity projections of consecutive through-focus scans encompassing the entire neuromast
685 of control and *sema7a*$^{-/-}$ mutant larvae at 2 dpf, 3 dfp, and 4 dpf were utilized to capture the
686 presynaptic and postsynaptic assemblies. The number of the synaptic densities across
687 genotypes were measured using ImageJ's cell counter framework. Area of the synaptic
688 densities from the maximal-intensity projections were measured using ImageJ's polygon
689 selection tool (Figure 6—figure supplement 2A-D).

690 **Quantification of the distribution of postsynaptic aggregates along the loops and the**
691 **bare terminals of the sensory arbor networks.** Four-day-old *TgBAC(neurod1:EGFP)* larvae
692 were fixed and stained for sensory arbors and postsynaptic aggregates marked by GFP and
693 MAGUK, respectively. The GFP-positive sensory arbors were traced in three dimensions with
694 ImageJ's semi-automated framework, SNT. The topological attributes of the arbor network,
695 such as the loop and the bare terminal, were determined as described previously. The
696 localizations of the MAGUK punctae along the three-dimensional arbor network were
697 measured using ImageJ's cell counter framework (Figure 6—figure supplement 2E,F). We
698 measured 567 MAGUK punctae from 16 sensory arbor networks. Whether the MAGUK-
699 punctae were associated with a loop or a bare terminal, we categorized them in two groups
700 and quantified their distribution across 16 neuromasts.

Quantification of the distribution of postsynaptic-aggregate density along the distance from the nearest node. The three-dimensional space surrounding each node of the arbor network were divided into concentric shells of equal volume (Figure 6—figure supplement 2E, F). For each node, we computationally generated 100,000 concentric shells that reached a 10 μm radius. We measured the number of MAGUK punctae located within each of those concentric shells from their nearest nodes.

Statistical analysis. Data visualization and statistical analysis were conducted with GraphPad Prism (Version 9) and Python (v3.10). The Mann-Whitney test was used for hypothesis testing unless otherwise noted, and the statistical details are given in the respective figure legends.

Data and code availability. Owing to size restrictions, the experimental image data have not been uploaded to a repository but are available from the corresponding author on request. The codes generated during this study are available on GitHub (https://github.com/agnikdasgupta/Sema7A_regulates_neural_circuitry).

Acknowledgments. The authors thank Nicolas Velez and Emily Atlas for valuable discussions. Samantha Campbell and Anna Kaczynska provided expert fish husbandry. Katie Kindt kindly provided various strains of zebrafish. Image processing benefitted from facilities at the Bio-Imaging Resource Center. A.D. was supported by a Kavli Neural Systems Institute Postdoctoral Fellowship from The Rockefeller University. C.C.R. is supported by National Science Foundation Graduate Research Fellowship Grant No. 1946429. A.J., S.P.P., and L.M.S. were supported by Howard Hughes Medical Institute, of which A.J.H. is an Investigator.

Author Contributions

A.D. initiated the project, conducted experiments, analyzed data, and quantified results. C.C.R developed the Python codes for the network topology analysis and quantified those results, as well as analyzed published transcriptomics data. S.P.P. developed the Python codes for three-dimensional visual representation of sensory arbors and quantified arbor morphologies. L.M.S.

726 conducted preliminary experiments. A.J. plotted Sema7A intensity measurements. A.D. wrote
727 the paper with contributions from C.C.R and A.J.H.

728 **Declaration of Interests**

729 The authors declare no competing interests.

730 **References**

731 1. Lykissas M, Batistatou A, Charalabopoulos K, Beris A. The Role of Neurotrophins in
732 Axonal Growth, Guidance, and Regeneration. Curr Neurovasc Res. 2007 May 1;4(2):143–
733 51.

734 2. Vaccaro G, Dumoulin A, Zuñiga NR, Bandtlow CE, Stoeckli ET. The Nogo-66 Receptors
735 NgR1 and NgR3 Are Required for Commissural Axon Pathfinding. J Neurosci. 2022 May
736 18;42(20):4087–100.

737 3. Nguyen-Ba-Charvet KT, Di Meglio T, Fouquet C, Chedotal A. Robos and Slits Control the
738 Pathfinding and Targeting of Mouse Olfactory Sensory Axons. J Neurosci. 2008 Apr
739 16;28(16):4244–9.

740 4. Jeroen Pasterkamp R, Peschon JJ, Spriggs MK, Kolodkin AL. Semaphorin 7A promotes
741 axon outgrowth through integrins and MAPKs. Nature. 2003 Jul;424(6947):398–405.

742 5. Nagiel A, Andor-Ardo D, Hudspeth AJ. Specificity of Afferent Synapses onto Plane-
743 Polarized Hair Cells in the Posterior Lateral Line of the Zebrafish. J Neurosci. 2008 Aug
744 20;28(34):8442–53.

745 6. Jacobo A, Dasgupta A, Erzberger A, Siletti K, Hudspeth AJ. Notch-Mediated Determination
746 of Hair-Bundle Polarity in Mechanosensory Hair Cells of the Zebrafish Lateral Line. Curr
747 Biol. 2019 Nov;29(21):3579-3587.e7.

748 7. Valera G, Markov DA, Bijari K, Randlett O, Asgharsharghi A, Baudoin JP, et al. A neuronal
749 blueprint for directional mechanosensation in larval zebrafish. Curr Biol. 2021
750 Apr;31(7):1463-1475.e6.

751 8. Dow E, Jacobo A, Hossain S, Siletti K, Hudspeth AJ. Connectomics of the zebrafish's
752 lateral-line neuromast reveals wiring and miswiring in a simple microcircuit. eLife. 2018 Jun
753 12;7:e33988.

754 9. Lush ME, Diaz DC, Koenecke N, Baek S, Boldt H, St Peter MK, et al. scRNA-Seq reveals
755 distinct stem cell populations that drive hair cell regeneration after loss of Fgf and Notch
756 signaling. eLife. 2019 Jan 25;8:e44431.

757 10. Carulli D, de Winter F, Verhaagen J. Semaphorins in Adult Nervous System Plasticity
758 and Disease. Front Synaptic Neurosci. 2021 May 11;13:672891.

759 11. Yazdani U, Terman JR. The semaphorins. Genome Biol. 2006;7(3):211.

760 12. de Winter F, Kwok JCF, Fawcett JW, Vo TT, Carulli D, Verhaagen J. The
761 Chemorepulsive Protein Semaphorin 3A and Perineuronal Net-Mediated Plasticity. Neural
762 Plast. 2016;2016:1–14.

763 13. Coate TM, Spita NA, Zhang KD, Isgrig KT, Kelley MW. Neuropilin-2/Semaphorin-3F-
764 mediated repulsion promotes inner hair cell innervation by spiral ganglion neurons. eLife.
765 2015 Aug 24;4:e07830.

766 14. Carcea I, Patil SB, Robison AJ, Mesias R, Huntsman MM, Froemke RC, et al.
767 Maturation of cortical circuits requires Semaphorin 7A. Proc Natl Acad Sci. 2014 Sep
768 23;111(38):13978–83.

769 15. Inoue N, Nishizumi H, Naritsuka H, Kiyonari H, Sakano H. Sema7A/PlxnCl signaling
770 triggers activity-dependent olfactory synapse formation. Nat Commun. 2018
771 Dec;9(1):1842.

772 16. Inoue N, Nishizumi H, Ooyama R, Mogi K, Nishimori K, Kikusui T, et al. The olfactory
773 critical period is determined by activity-dependent Sema7A/PlxnC1 signaling within
774 glomeruli. eLife. 2021 Mar 29;10:e65078.

775 17. Morote-Garcia JC, Napiwotzky D, Köhler D, Rosenberger P. Endothelial Semaphorin
776 7A promotes neutrophil migration during hypoxia. Proc Natl Acad Sci. 2012 Aug
777 28;109(35):14146–51.

778 18. Nishide M, Kumanogoh A. The role of semaphorins in immune responses and
779 autoimmune rheumatic diseases. Nat Rev Rheumatol. 2018 Jan;14(1):19–31.

780 19. Köhler D, Granja T, Volz J, Koeppen M, Langer HF, Hansmann G, et al. Red blood
781 cell-derived semaphorin 7A promotes thrombo-inflammation in myocardial ischemia-
782 reperfusion injury through platelet GPIb. Nat Commun. 2020 Dec;11(1):1315.

783 20. Pham TL, He J, Kakazu AH, Jun B, Bazan NG, Bazan HEP. Defining a mechanistic
784 link between pigment epithelium–derived factor, docosahexaenoic acid, and corneal nerve
785 regeneration. J Biol Chem. 2017 Nov;292(45):18486–99.

786 21. Xie J, Wang H. Semaphorin 7A as a potential immune regulator and promising
787 therapeutic target in rheumatoid arthritis. Arthritis Res Ther. 2017 Dec;19(1):10.

788 22. Baek S, Tran NTT, Diaz DC, Tsai YY, Acedo JN, Lush ME, et al. Single-cell
789 transcriptome analysis reveals three sequential phases of gene expression during
790 zebrafish sensory hair cell regeneration. Dev Cell. 2022 Mar 28;57(6):799-819.e6.

791 23. Dow E, Siletti K, Hudspeth AJ. Cellular projections from sensory hair cells form
792 polarity-specific scaffolds during synaptogenesis. Genes Dev. 2015 May 15;29(10):1087–
793 94.

794 24. Pujol-Martí J, Faucherre A, Aziz-Bose R, Asgharsharghi A, Colombelli J, Trapani JG,
795 et al. Converging Axons Collectively Initiate and Maintain Synaptic Selectivity in a
796 Constantly Remodeling Sensory Organ. Curr Biol. 2014 Dec;24(24):2968–74.

797 25. De Wit J, De Winter F, Klooster J, Verhaagen J. Semaphorin 3A displays a punctate
798 distribution on the surface of neuronal cells and interacts with proteoglycans in the
799 extracellular matrix. Mol Cell Neurosci. 2005 May;29(1):40–55.

800 26. Dalle Nogare DE, Natesh N, Vishwasrao HD, Shroff H, Chitnis AB. Zebrafish Posterior
801 Lateral Line primordium migration requires interactions between a superficial sheath of
802 motile cells and the skin. eLife. 2020 Nov 25;9:e58251.

803 27. Ji YR, Warrier S, Jiang T, Wu DK, Kindt KS. Directional selectivity of afferent neurons
804 in zebrafish neuromasts is regulated by Emx2 in presynaptic hair cells. eLife. 2018 Apr
805 19;7:e35796.

806 28. Diaz-Horta O, Abad C, Sennaroglu L, Foster J, DeSmidt A, Bademci G, et al. ROR1 is
807 essential for proper innervation of auditory hair cells and hearing in humans and mice. Proc
808 Natl Acad Sci U S A. 2016 May 24;113(21):5993–8.

809 29. Newman M. The structure of real-world networks [Internet]. Vol. 1. Oxford University
810 Press; 2018 [cited 2023 May 2]. Available from:
811 https://academic.oup.com/book/27884/chapter/203817512

812 30. Sharma P, Ruel TD, Kocha KM, Liao S, Huang P. Single cell dynamics of embryonic
813 muscle progenitor cells in zebrafish. Development. 2019 Jan 1;dev.178400.

814 31. Keenan SR, Currie PD. The Developmental Phases of Zebrafish Myogenesis. J Dev
815 Biol. 2019 Jun 2;7(2):12.

816 32. Sato A, Koshida S, Takeda H. Single-cell analysis of somatotopic map formation in the
817 zebrafish lateral line system. Dev Dyn. 2010 Jul;239(7):2058–65.

818 33. Shen K, Cowan CW. Guidance Molecules in Synapse Formation and Plasticity. Cold
819 Spring Harb Perspect Biol. 2010 Apr 1;2(4):a001842–a001842.

820 34. Um JW, Ko J. Neural Glycosylphosphatidylinositol-Anchored Proteins in Synaptic
821 Specification. Trends Cell Biol. 2017 Dec;27(12):931–45.

822 35. Uesaka N, Uchigashima M, Mikuni T, Nakazawa T, Nakao H, Hirai H, et al. Retrograde
823 semaphorin signaling regulates synapse elimination in the developing mouse brain.
824 Science. 2014 May 30;344(6187):1020–3.

825 36. Sheets L, Hagen MW, Nicolson T. Characterization of Ribeye Subunits in Zebrafish
826 Hair Cells Reveals That Exogenous Ribeye B-Domain and CtBP1 Localize to the Basal
827 Ends of Synaptic Ribbons. Riley B, editor. PLoS ONE. 2014 Sep 10;9(9):e107256.

828 37. Oliva C, Escobedo P, Astorga C, Molina C, Sierralta J. Role of the maguk protein
829 family in synapse formation and function. Dev Neurobiol. 2012 Jan;72(1):57–72.

830 38. Suli A, Pujol R, Cunningham DE, Hailey DW, Prendergast A, Rubel EW, et al.
831 Innervation regulates synaptic ribbons in lateral line mechanosensory hair cells. J Cell Sci.
832 2016 Jan 1;jcs.182592.

833 39. Obholzer N, Wolfson S, Trapani JG, Mo W, Nechiporuk A, Busch-Nentwich E, et al.
834 Vesicular Glutamate Transporter 3 Is Required for Synaptic Transmission in Zebrafish Hair
835 Cells. J Neurosci. 2008 Feb 27;28(9):2110–8.

836 40. Taschenberger H, Leão RM, Rowland KC, Spirou GA, von Gersdorff H. Optimizing
837 Synaptic Architecture and Efficiency for High-Frequency Transmission. Neuron. 2002
838 Dec;36(6):1127–43.

839 41. Myers JP, Gomez TM. Focal Adhesion Kinase Promotes Integrin Adhesion Dynamics
840 Necessary for Chemotropic Turning of Nerve Growth Cones. J Neurosci. 2011 Sep
841 21;31(38):13585–95.

842 42. O'Donnell M, Chance RK, Bashaw GJ. Axon Growth and Guidance: Receptor
843 Regulation and Signal Transduction. Annu Rev Neurosci. 2009 Jun 1;32(1):383–412.

844 43. Gilmour D, Knaut H, Maischein HM, Nüsslein-Volhard C. Towing of sensory axons by
845 their migrating target cells in vivo. Nat Neurosci. 2004 May;7(5):491–2.

846 44. Metcalfe WK. Sensory neuron growth cones comigrate with posterior lateral line
847 primordial cells in zebrafish. J Comp Neurol. 1985 Aug 8;238(2):218–24.

848 45. Gasanov EV, Rafieva LM, Korzh VP. BDNF-TrkB Axis Regulates Migration of the
849 Lateral Line Primordium and Modulates the Maintenance of Mechanoreceptor Progenitors.
850 Proost P, editor. PLOS ONE. 2015 Mar 9;10(3):e0119711.

851 46. Schuster K, Dambly-Chaudière C, Ghysen A. Glial cell line-derived neurotrophic factor
852 defines the path of developing and regenerating axons in the lateral line system of
853 zebrafish. Proc Natl Acad Sci. 2010 Nov 9;107(45):19531–6.

854 47. Germanà A, Laurà R, Montalbano G, Guerrera MC, Amato V, Zichichi R, et al.
855 Expression of Brain-Derived Neurotrophic Factor and TrkB in the Lateral Line System of
856 Zebrafish During Development. Cell Mol Neurobiol. 2010 Jul;30(5):787–93.

857 48. Kindt KS, Finch G, Nicolson T. Kinocilia Mediate Mechanosensitivity in Developing
858 Zebrafish Hair Cells. Dev Cell. 2012 Aug;23(2):329–41.

859 49. Kwan KM, Fujimoto E, Grabher C, Mangum BD, Hardy ME, Campbell DS, et al. The
860 Tol2kit: A multisite gateway-based construction kit forTol2 transposon transgenesis
861 constructs. Dev Dyn. 2007 Nov;236(11):3088–99.

862 50. Arshadi C, Günther U, Eddison M, Harrington KIS, Ferreira TA. SNT: a unifying
863 toolbox for quantification of neuronal anatomy. Nat Methods. 2021 Apr;18(4):374–7.

864

865 **Figures and Figure Legends**

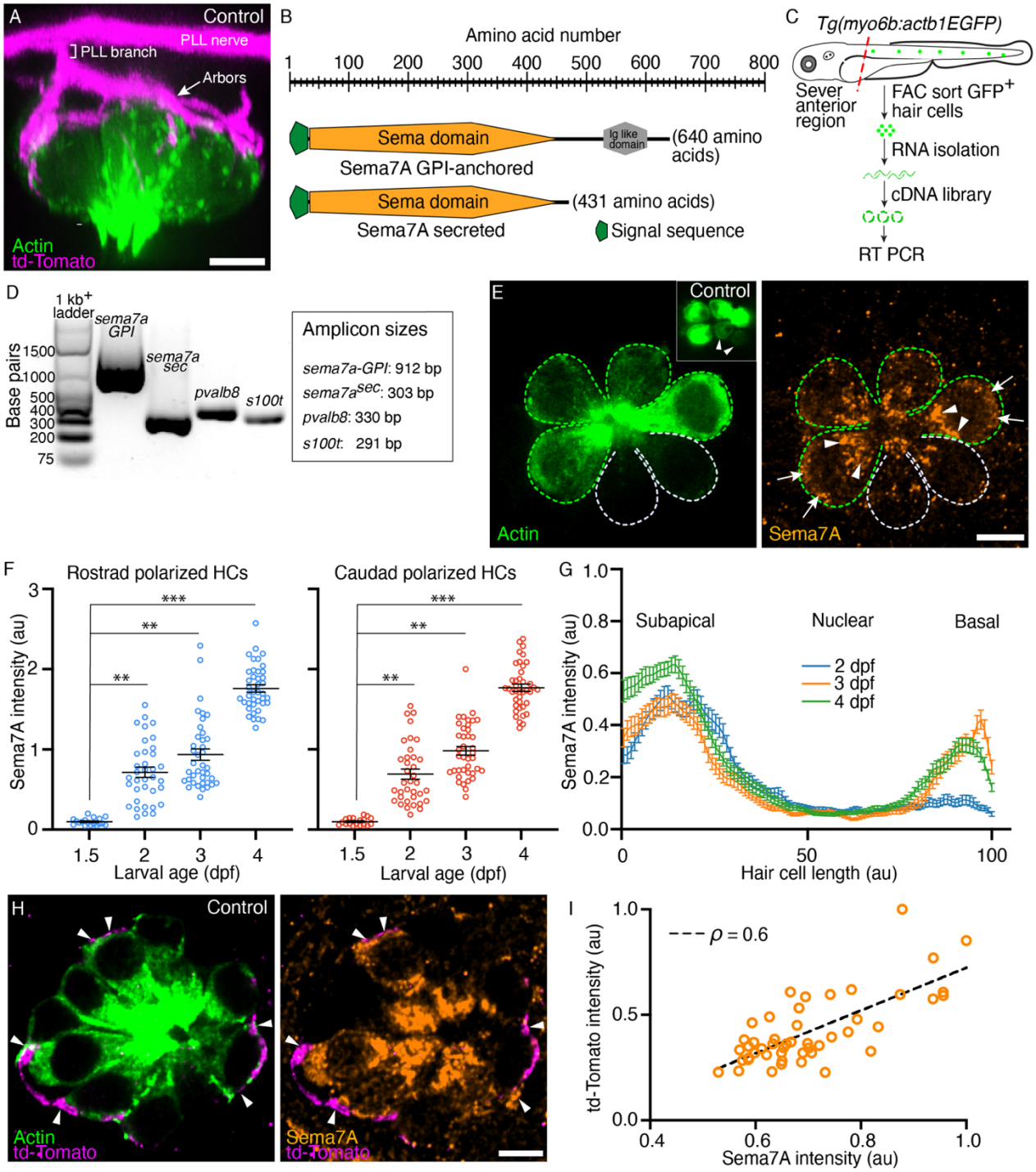

866 **Figure 1. Expression of Semaphorin7A in the zebrafish's lateral line.** (A) A volumetric
867 rendering of a PLL neuromast depicts the sensory axons (magenta) that branch from the lateral
868 line nerve to arborize around the basolateral surface of the hair cell cluster (green). Additional
869 cell types in the neuromast are not labeled. Larval age, 3 dpf. (B) A schematic drawing of the

870 two variants of the Sema7A protein molecule depicts the full-length GPI-anchored form and the
871 smaller, potentially secreted form. Both the molecules include a signal sequence (green) and
872 a conserved sema domain (orange). (C) *Tg(myo6b:actb1-EGFP)* larvae at 4 dpf were
873 terminally anesthetized and their heads were removed with fine blades. The tails were then
874 dissociated into the component cells, which were sorted by flow cytometry. Green cells
875 represent GFP^+ hair cells. A cDNA library was prepared from the isolated RNA. (D) Gel-based
876 RT-PCR analysis indicates the presence of both the *sema7a* transcript variants and the
877 expression of hair cell-specific genes, parvalbumin 8 (*pvalb8*) and S100 calcium binding
878 protein T (*s100t*). (E) A surface micrograph of a neuromast at 3 dpf depicts two pairs of mature
879 hair cells (green dashed lines) and a pair of immature hair cells (grey dashed lines). Inset:
880 among the three pairs of hair cell apices, the immature pair is indicated by arrowheads.
881 Immunolabeling reveals that the Sema7A protein (orange) occurs consistently at the subapical
882 region (arrowheads) and at the basolateral surface (arrows) of a hair cell. In this and in each
883 of the subsequent neuromast images, anterior is to the left and dorsal to the top. (F) A plot
884 quantifies developmental changes in the average Sema7A intensity in both rostrally and
885 caudally polarized hair cells of neuromasts from 1.5 dpf to 4 dpf. The data stem from 18, 36,
886 39, and 40 hair cells in neuromasts of respectively 1.5 dpf, 2 dpf, 3 dpf, and 4 dpf larvae. (G) A
887 plot quantifies the distribution of average Sema7A intensity along the hair cell's apicobasal
888 axis. The results stem from 52, 57, and 54 hair cells of neuromasts from 2 dpf, 3 dpf, and 4 dpf
889 larvae. (H) An immunofluorescence image at the nuclear level of a 4 dpf neuromast shows the
890 contact of the sensory arbors (magenta) with the basolateral surface of the hair cells (green).
891 Immunolabeling for Sema7A (orange) reveals enrichment of the protein at the hair cell bases
892 and sensory-axon interfaces (arrowheads). (I) At the base of the hair cell, association of the td-
893 $Tomato^+$ sensory arbors positively correlated with the Sema7A intensity. The results stemmed
894 from 48 hair cells of 13 neuromasts from 3 dpf larvae. HC, hair cell; scale bars, 5 μm; au,
895 arbitrary unit; means ± SEMs; ρ, Spearman's correlation coefficient; *** implies $p < 0.001$ and
896 ** implies $p < 0.01$.
897

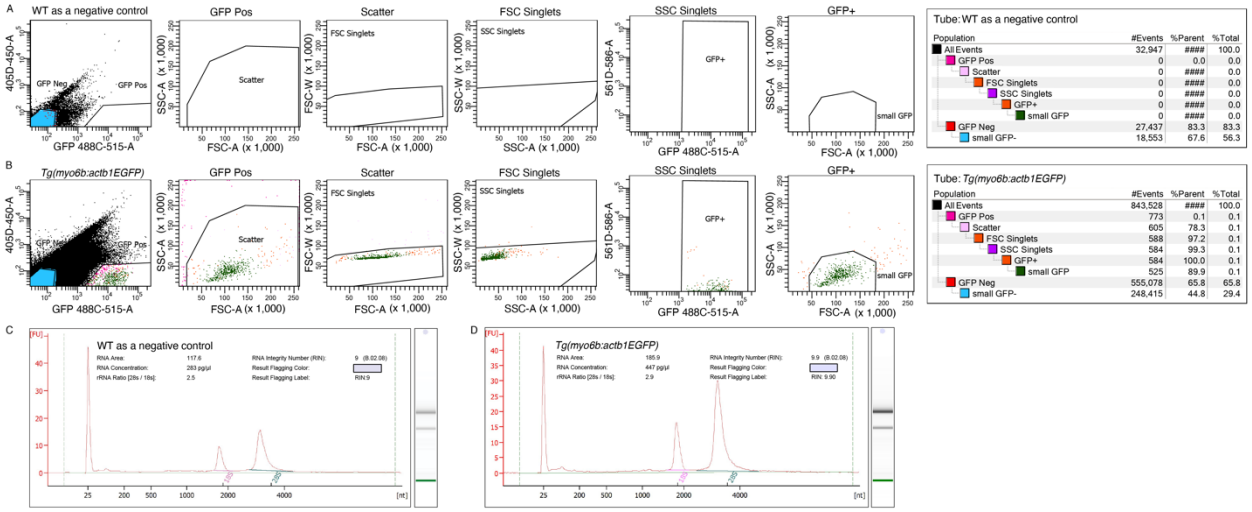

Figure 1—figure supplement 1. Isolation of GFP-expressing hair cells. (A,B) Representative results from florescence-activated cell sorting demonstrate the efficient discrimination of GFP+ (green) hair cells from *Tg(myo6b:actb1-EGFP)* larval tails. Around 400 tails were utilized to isolate hair cells. Wild type (WT) controls confirm the selectivity of the gates. (C,D) Plots represent the RNA integrity numbers (RINs) of the isolated total RNA from WT and transgenic larvae. High RIN values suggest minimal degradation of isolated RNAs from both samples.

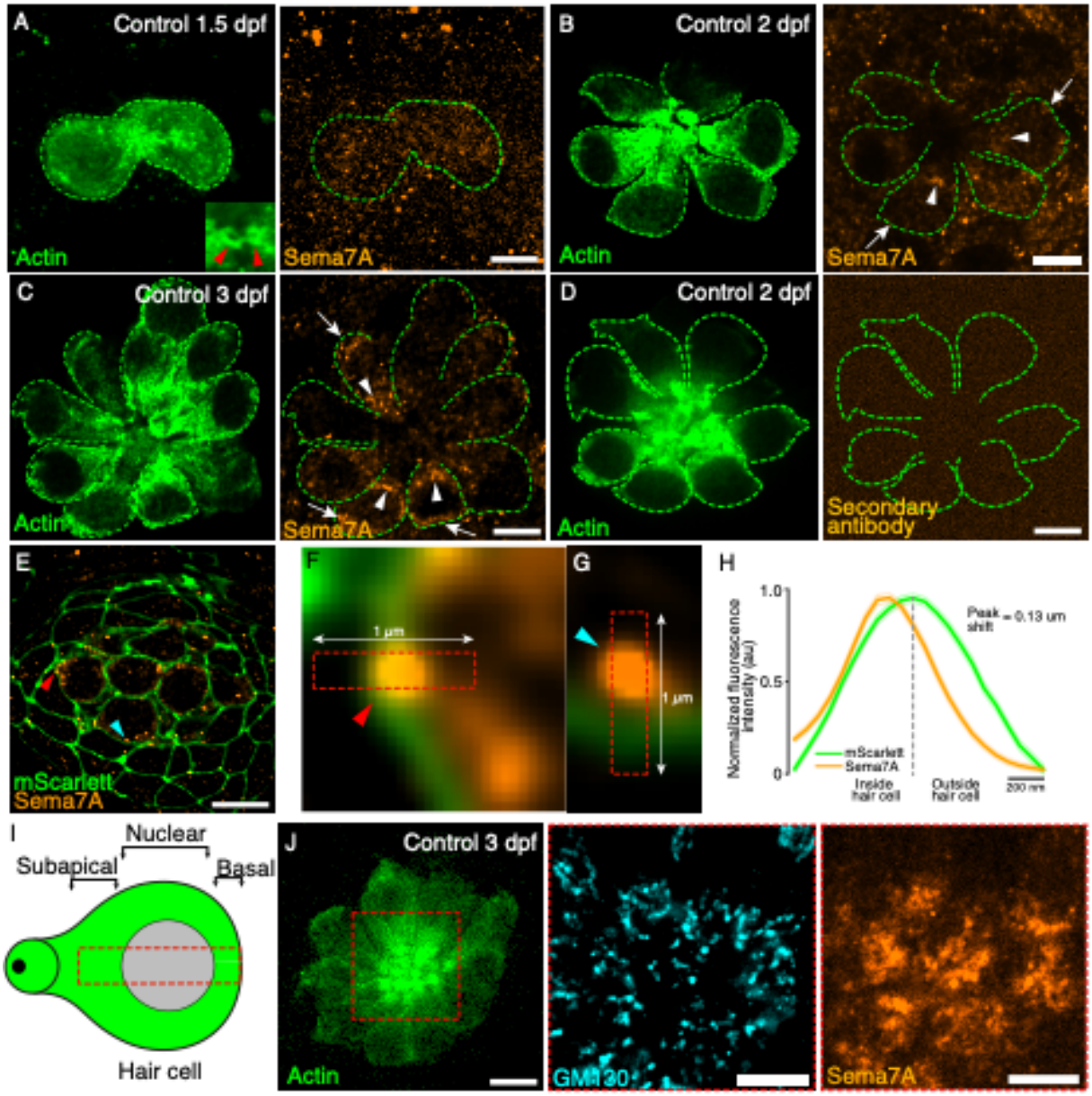

906

907 **Figure 1—figure supplement 2. Expression of Semaphorin7A in the lateral line**
908 **neuromast.** (A-C) Surface micrographs show hair cells marked with actin-GFP (green dashed
909 lines) and the localization of Sema7A protein (orange) in the subapical (arrowheads) and basal
910 regions (arrows) of the corresponding hair cells from neuromasts of developing control larvae.
911 The inset in panel A (red arrowheads) depicts the apices of the immature hair cell pair.
912 (D) Immunolabeling with only the secondary antibody fails to detect any Sema7A signal. (E) A
913 micrograph at a nuclear plane of a 4 dpf neuromast depicts membrane-tethered Scarlet (green)
914 in all cells of the neuromast and the Sema7A protein (orange, arrowheads) in centrally
915 clustered hair cells. (F) The Sema7A protein is located at the basal membrane (red arrowhead).

916 (G) The Sema7A protein is also observed adjacent to the basal membrane, potentially in a
917 vesicle (cyan arrowhead). (H) A plot quantifies the distribution of average Sema7A intensity
918 across the hair cell's basal membrane. The results stem from 100 hair-cell membranes of 10
919 neuromasts from 4 dpf larvae. (I) A schematic diagram of a single hair cell depicts the three
920 distinct regions along the apicobasal axis of the cell. Sema7A intensity was measured along
921 this apicobasal axis (red dashed line). (J). A surface micrograph depicts hair cells (green, left)
922 whose subapical region (red dashed line) harbors the Golgi network (cyan, middle) where the
923 Sema7A protein is enriched (orange, right). Scale bars, 5 μm; au, arbitrary unit;
924 means ± SEMs.
925

926

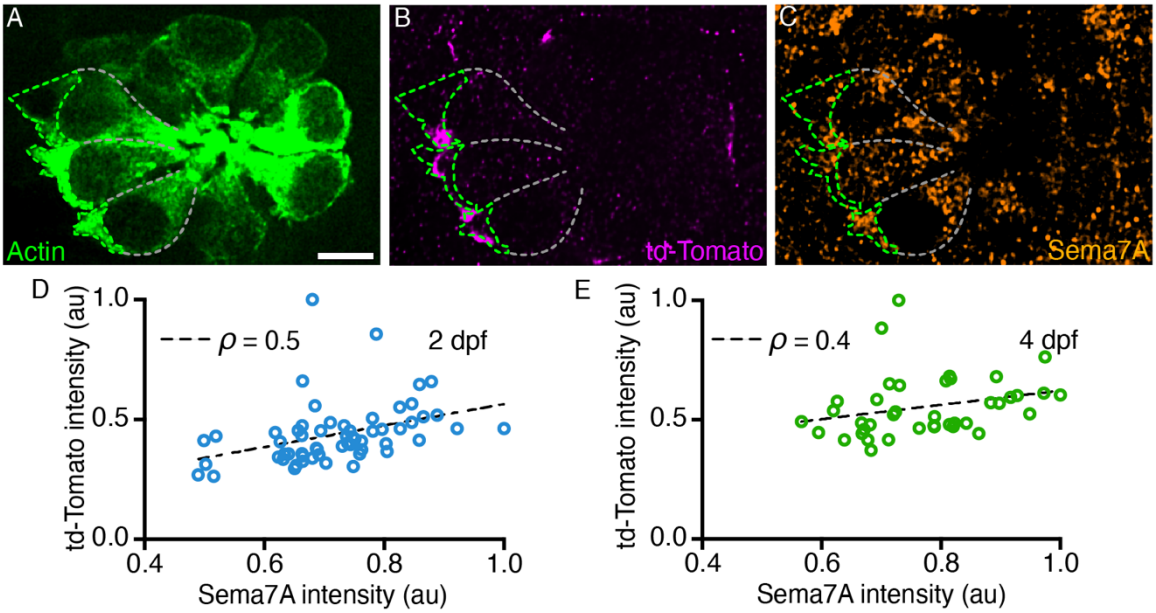

927 **Figure 1—figure supplement 3. Sema7A progressively enriches at the hair cell base with**
928 **the sensory axons.** (A) A micrograph at a nuclear plane of a 3 dpf neuromast depicts several
929 actin-GFP (green) labeled hair cells. The lateral (white dashed line) and the basal (green
930 dashed line) surfaces of three hair cells are outlined. (B) The td-Tomato$^+$ sensory arbors
931 contact the basal regions (green dashed line) of three hair cells. (C) The Sema7A is enriched
932 in the basal regions (green dashed line) of the hair cells that are in contact with the sensory
933 arbors. (D,E) At the base of the hair cell, intensities of the td-Tomato$^+$ sensory arbors positively
934 correlate with the Sema7A intensities. The results stem from 66 hair cells of 15 neuromasts
935 from 2 dpf larvae and 40 hair cells of 11 neuromasts from 4 dpf larvae. Scale bars, 5 μm; au,
936 arbitrary unit; ρ, Spearman's correlation coefficient.
937

```
Mus             MTPPPPGRAAPSAPRARVLSLPARFGLPLRLRLLLVFWVAAASAQGHSRSGPRISAVWKG
Danio           -------------------MIRHYSSLKFKGNLAYPWLIYGACFQCVFCSCNPRLTLKQD
                                    :    .* :: .*   : : .*. *    *     :: :.

Mus             QDHVDFSQPEPHTVLFHEPGSFSVWVGGRGKVYHFNFPEGKNASVRTVNIGSTKGSCQDK
Danio           NAPLNYNTNYSHTVLFHEEGSKSLFVGGSNIVLHFDVDSYEILENFTLNANLPR---CGE
                :  :::.   .******* ** *::*** . * **:. . :  .  *:* . .:    .:

Mus             QDCGNYITLLERRGNGLLVCGTNARKPSCWNLVN---DSVMMSLGEMKGYAPFSPDENSL
Danio           SSCENVVTVIETFQNCKFVCGTNGEEPQCWELYPRESNHSVVKSVEGTGISPHSSEQNSL
                ..* * :*::*   *  :*****..:*.**:*     :  ::.  * .* :*.*.::***

Mus             VLFEGDEVYSTIRKQEYNGKIPRFRRIRGESELYTSDTVMQNPQFIKATIVH-QDQAYDD
Danio           SLVADGDLYAAAPLYSDGTLLQFRRKAGKRINVWMHDQWVSEPTFISSFLAKRKNDSLNE
                 *. ..::*::    . .  :   *:   . :::  *  :.:* **.: :.: :::: ::

Mus             KIYYFFREDNPDKNPEAPLNVSRVAQLCRGDQGGESSLSVSKWNTFLKAMLVCSDAATNR
Danio           KIYVLFREKNSDTSPEADPWISRVARVCKIDEGGSKQFLQNIWTSFLKARLVCGIPKESL
                *** :***.*.*..***   :****::*: *:**...:  . *.:**** ***. .  .

Mus             NFNRLQDVFLLPDPSGQWRDTRVYGVFSNPWNYSAVCVYSLGDIDRVFRTSSLKGYHMGL
Danio           YFNRLQDVFVQH--AEDWRDSLVYALFSSSWNSTAVCIYSLADLDDIFEKSNYKGFSEAI
                 ********:    : :***: **.:**..** :***:***.*:* :*..*. **:  .:

Mus             PNPRPGMCLPKKQPIPTETFQVADSHPEVAQRVEPMGPLKTPLFHSKYHYQKVVVHRMQA
Danio           PNPRPGKCVENSNSLPIPTLKIIKDYPEMKDWIHPIQ-KDTPFFTSSKNFTKIVVDQIRA
                ****** *: :.:.:*  *::: ..:**: : :.*:   .**:* *. :: *:**.:::*

Mus             SNGETFHVLYLTTDRGTIHKVVESGDQDHSFVFNIMEIQPFHRAAAIQAISLDADRRKLY
Danio           LDENVYNVLLLATDDGMIFKILQHG----SKPFIISETHLCNGCAPIQSMKLDSKKRKLF
                 : :.::** *:** * *.*::: *    *  * * * :  : .*.**::.**:.:***:

Mus             VTSQWEVSQVPLDMCEVYSGGCHGCLMSRDPYCGWDQDRCVSIYSS--QRSVLQSINPAE
Danio           VGYPGQMSVLELQRCQDYGASCEECVLSRDPYCAWSEKGCTSQTRGGIQNISDGNVTKVC
                *    ::* : *: *: *...*. *::******.*.:. *.*   .  *.    .:. .

Mus             PHRECPNPKPDE------APLQKVSLARNSRYYLTCPMESRHATYLWRHEENVEQSCEPG
Danio           DHKSVGRVRRDAQQSSTAPSRIQHTVATDVPFYLSCPVDSHHASYRWEHGG---KSNPCQ
                 *:.  . : *       ..  : ::* :  :**:**::*:**:* *.*     :*

Mus             HQSPSCILFIENLTARQYGHYRCEAQEGSYLREAQHWELLPE-DRALAEQLMGHARALAA
Danio           QTQSEYLLLIPAMTAENYGNYSCVSQERDYIKVVREYELLAKSVFNDAFKLKIQDRQLMV
                : ... :*:*  :**.:**:* * :** .*:: .:.:***.:     * :*  : * * .

Mus             SFWLGVLPTLILGLLVH
Danio           AFVTSAFYLCSL-----
                :*  ..:    *
```

Sequence 1: Mus musculus 664 aa
Sequence 2: Danio rerio 640 aa
Immunogen: Mouse myeloma cell line NS0-derived recombinant mouse Semaphorin 7A Glutamine 45-Alanine 646, which corresponds to the Glutamine 26-Methionine 627 of zebrafish Semaphorin 7A. We predict that the antibody recognizes both variants of the *sema7a* encoded proteins. The Sema domains in both mouse and zebrafish are highlighted in orange.

Figure 1—figure supplement 4. Alignment of the mouse and the zebrafish Sema7A protein sequences generated by Clustal Omega. (A) Multiple sequence alignment depicts the conserved Sema domain (orange) and the immunogenic region for the Sema7A antibody in mouse, and its equivalent region in zebrafish.

943 **Video 1. Sema7A is enriched at the hair cell base and sensory-axon interface**. A through-
944 focus scan of a 4 dpf control neuromast depicts the hair cells (green) that are innervated by the
945 sensory axons (magenta) at their basolateral surfaces where the Sema7A protein (orange) is
946 highly enriched. Scale bar, 5 μm.
947

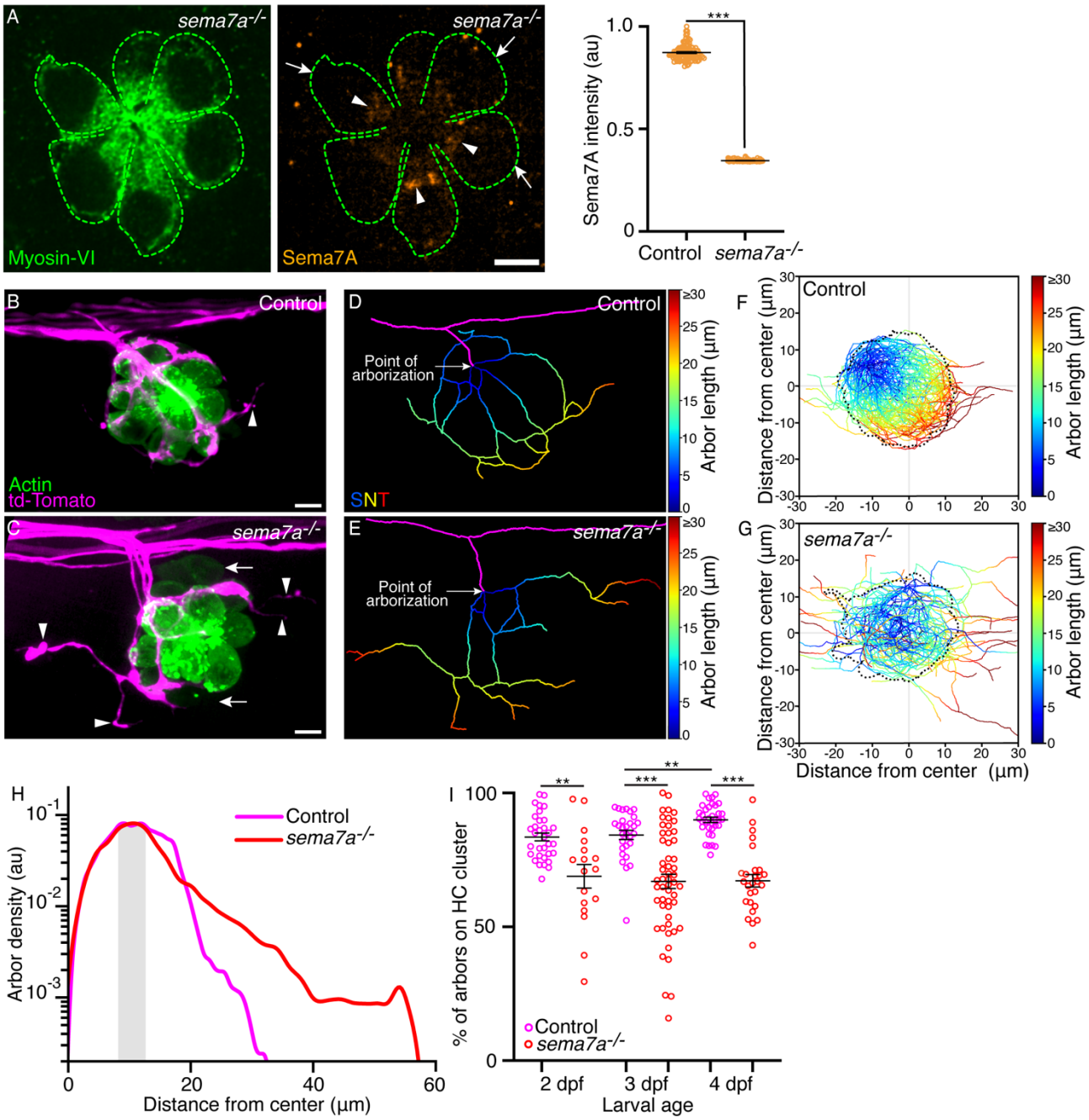

948 **Figure 2. *sema7a*$^{-/-}$ mutants display aberrant sensory axon arborizations.** (A) In a
949 micrograph of a 3 dpf *sema7a*$^{-/-}$ neuromast, Myosin VI (green) marks the hair cells (green
950 dashed lines) in which the level of Sema7A (orange) is highly reduced, with sporadic
951 localization in the subapical region (arrowheads) and none in the basolateral (arrow) region. A
952 plot of normalized Sema7A intensity from 99 control and 100 *sema7a*$^{-/-}$ hair cells quantitates
953 the effect. (B,C) Surface views of a control and a *sema7a*$^{-/-}$ neuromast at 4 dpf depict the

954 interaction of the sensory arbors (magenta) with hair cell clusters (green). In the control, the
955 arbors intimately contact the hair cells, with a few exceptions (arrowhead). In the *sema7a*$^{-/-}$
956 mutant, the arbors direct many aberrant projections (arrowheads) away from the hair cell
957 cluster. The two immature hair cell pairs in the *sema7a*$^{-/-}$ neuromast are indicated by arrows.
958 (D,E) Skeletonized networks portray the three-dimensional topology of the sensory arbors from
959 the control and the *sema7a*$^{-/-}$ neuromasts depicted in panels B and C. The pseudocolored
960 trajectories depict the increase in arbor contour length from each point of arborization, defined
961 as the point at which the lateral line branch (magenta) contacts hair cell cluster.
962 (F,G) Micrographs depict the skeletonized networks of the combined 4 dpf hair cell clusters,
963 whose centers are located at (0,0). The X- and Y-coordinates represent the anteroposterior
964 (AP) and the dorsoventral (DV) axes of the larva, respectively. Positive values of the X- and
965 Y-coordinates represent the posterior and ventral directions, respectively. Combined
966 skeletonized network traces from 27 control and 27 *sema7a*$^{-/-}$ mutant neuromasts are
967 represented. H) The plot denotes the densities of the sensory arbors around the center of the
968 combined hair cell clusters for 35 control (magenta) and 27 *sema7a*$^{-/-}$ (red) neuromasts at 4 dpf.
969 The shaded area marks the region proximal to the boundary of the combined hair cell cluster.
970 (I) The plot quantifies the degree of contact of the sensory arbors to their hair cell clusters in
971 individual neuromasts from both control (magenta) and *sema7a*$^{-/-}$ mutants (red), each point
972 represents a single neuromast. Thirty-three, 29, and 35 neuromasts were analyzed from 2 dpf,
973 3 dpf, and 4 dpf control larvae, respectively. Seventeen, 53, and 27 neuromasts were analyzed
974 from 2 dpf, 3 dpf, and 4 dpf *sema7a*$^{-/-}$ mutant larvae, respectively. HC, hair cell; Scale bars,
975 5 μm; au, arbitrary unit; means ± SEMs; *** signifies $p < 0.001$; ** signifies $p < 0.01$.
976

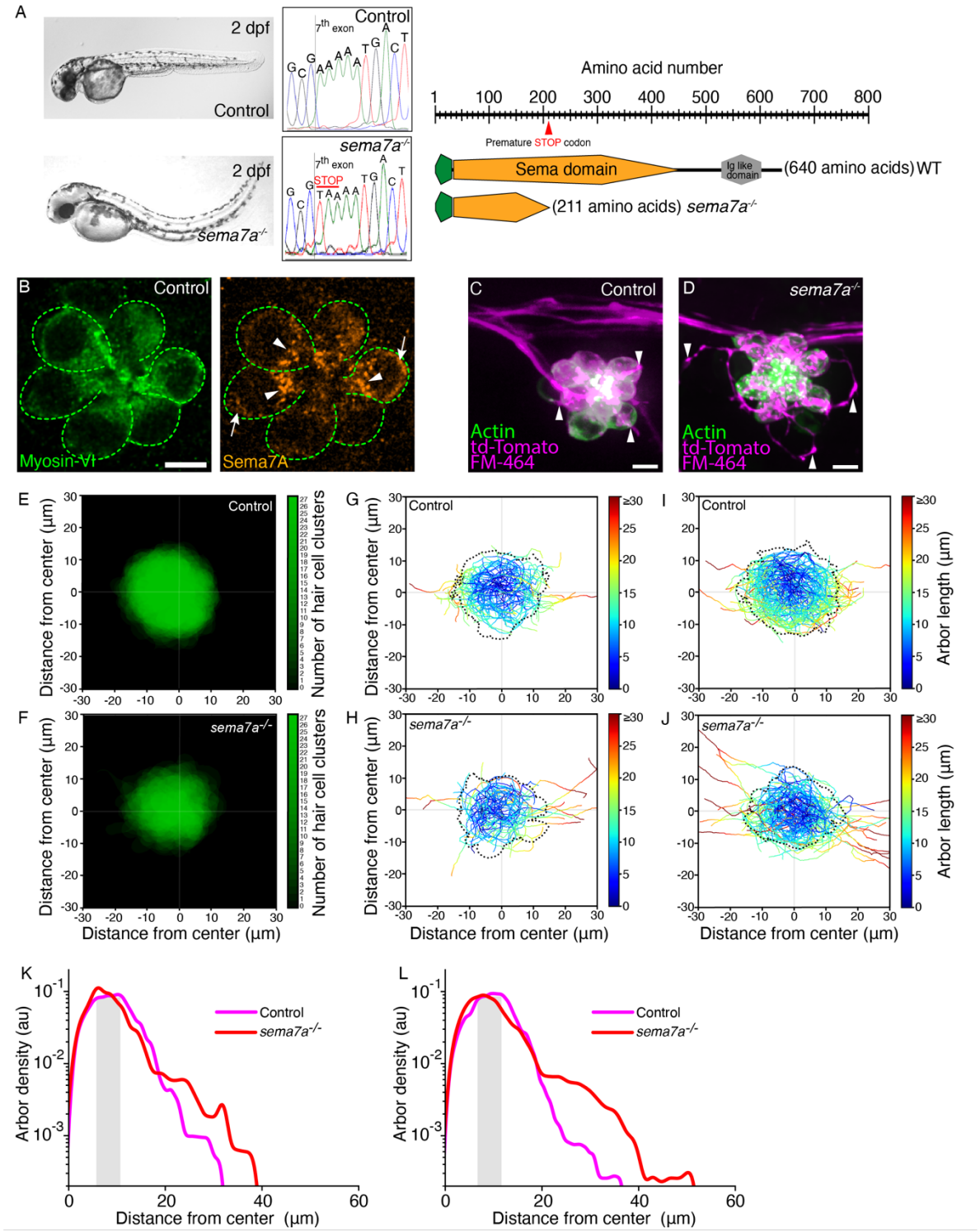

Figure 2—figure supplement 1. *sema7a*$^{-/-}$ mutants exhibit aberrant sensory-axon arborization throughout development. (A) Micrographs depict the overall morphologies and *sema7a* genomic profiles of 2 dpf control (top) and *sema7a*$^{-/-}$ larvae (bottom). The schematic diagram on the right depicts the mutation site and the resulting early truncation of the encoded

983 protein. (B) In a surface micrograph of a 3 dpf control neuromast, myosin VI (green) marks hair
984 cells (green dashed lines). Sema7A (orange) protein is highly enriched in the subapical region
985 (arrowheads) and basolateral (arrows) region of the hair cells. (C,D) Micrographs depict
986 maximum intensity projections of 4 dpf neuromasts from control and *sema7a*$^{-/-}$ larvae where
987 the hair cells (green) are stained with FM4-64 (magenta). The sensory arbors (arrowheads,
988 magenta) tightly enwrap the clustered hair cells in the control neuromast but show aberrant
989 arborization in the *sema7a*$^{-/-}$ larvae. (E,F) Micrographs depict combined 4 dpf hair cell clusters,
990 each of whose centers arise located at (0,0). The X- and Y-coordinates represent the
991 anteroposterior (AP) and dorsoventral (DV) axes of the larva, respectively. Positive values of
992 the X- and Y-coordinates represent posterior and ventral directions, respectively. Combined
993 hair cell clusters from 27 control and 27 *sema7a*$^{-/-}$ mutant neuromasts are represented.
994 (G,H) Micrographs depict the skeletonized networks of the combined 2 dpf hair cell clusters
995 from 17 control and 17 *sema7a*$^{-/-}$ mutant neuromasts. (I,J) Micrographs depict the skeletonized
996 networks of the combined 3 dpf hair cell clusters from 29 control and 29 *sema7a*$^{-/-}$ mutant
997 neuromasts. (K) A plot quantitates the densities of the sensory arbors around the center of the
998 combined hair cell clusters for 33 control (magenta) and 17 *sema7a*$^{-/-}$ (red) neuromasts at 2 dpf.
999 The shaded area marks the region proximal to the boundary of the combined hair cell cluster.
1000 (L) A plot quantitates the densities of the sensory arbors around the center of the combined
1001 hair cell clusters for 29 control (magenta) and 53 *sema7a*$^{-/-}$ (red) neuromasts at 3 dpf. The
1002 shaded area marks the region proximal to the boundary of the combined hair cell cluster. Scale
1003 bars, 5 μm; au, arbitrary units.
1004

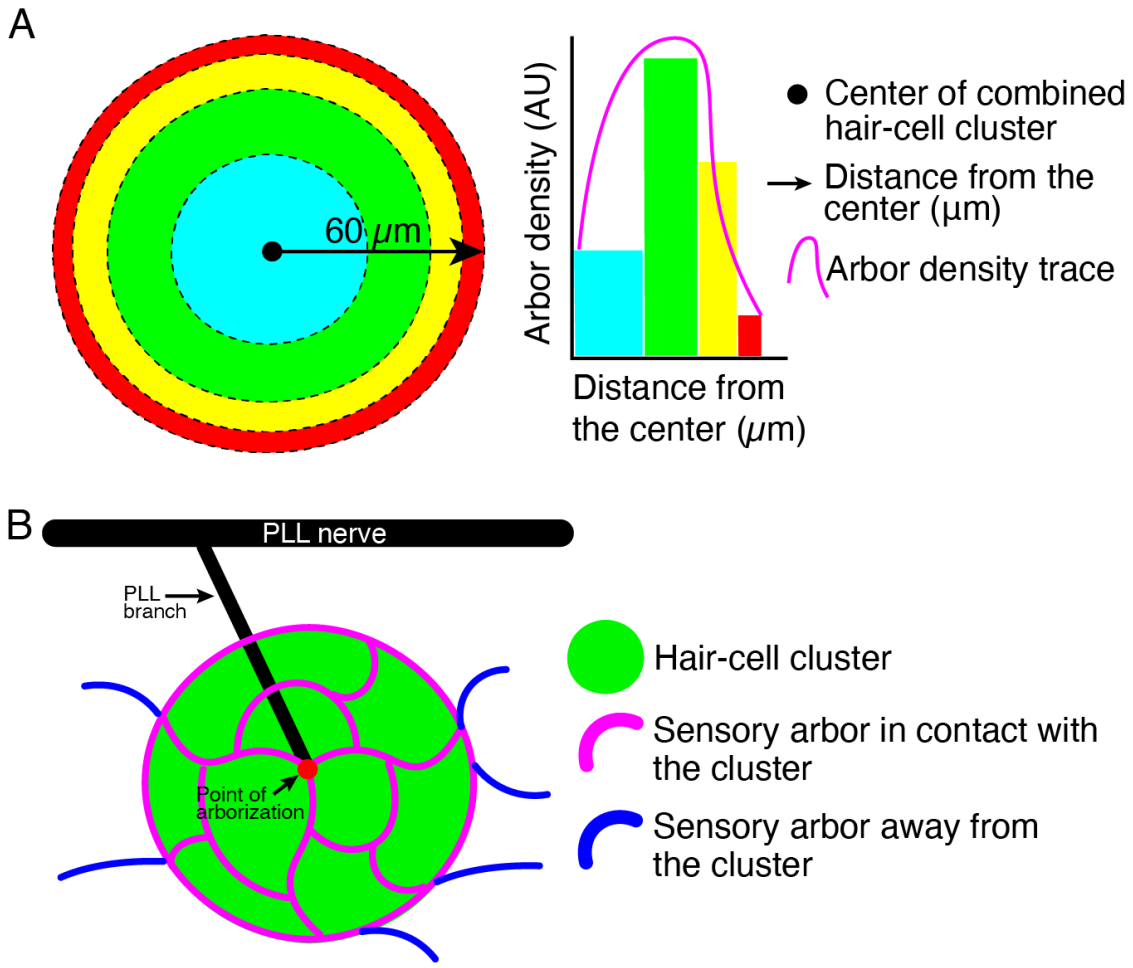

Figure 2—figure supplement 2. Quantification of sensory arbor distributions and contacts with hair cell clusters. (A) A schematic drawing of the combined hair cell cluster and surrounding region depicts concentric sections of equal area in distinct colors (cyan, green, yellow, and red). The arbor density is plotted as a histogram against the distance (black arrow) from the center (black circle) of the combined hair cell cluster. The histogram is represented as a density trace graph (magenta). (B) A schematic drawing of a posterior lateral-line neuromast depicts the posterior lateral-line (PLL) nerve (black), posterior lateral-line branch (black), the point or arborization, the sensory arbors (magenta) that contact the hair cell cluster (green), and the sensory arbors that project away (blue) from the hair cell cluster.

1015 **Videos 2 and 3. FM4-64 labels the hair cells of both control and *sema7a*$^{-/-}$ mutant**
1016 **neuromasts**. Through-focus scans of 4 dpf control (Video 2) and *sema7a*$^{-/-}$ mutant (Video 3)
1017 neuromasts depict the hair cells (green) that have incorporated FM4-64. The sensory arbors
1018 (magenta) are tightly associated with the clustered hair cells in the control neuromast but show
1019 aberrant arborization in the *sema7a*$^{-/-}$ larvae.

1020 **Video 4. Three-dimensional arborization patterns in control and *sema7a*$^{-/-}$ neuromasts.**
1021 Lateral views depict **t**hree-dimensionally rendered combined skeletonized network traces from
1022 27 control and 27 *sema7a*$^{-/-}$ mutant neuromasts at 4 dpf.
1023

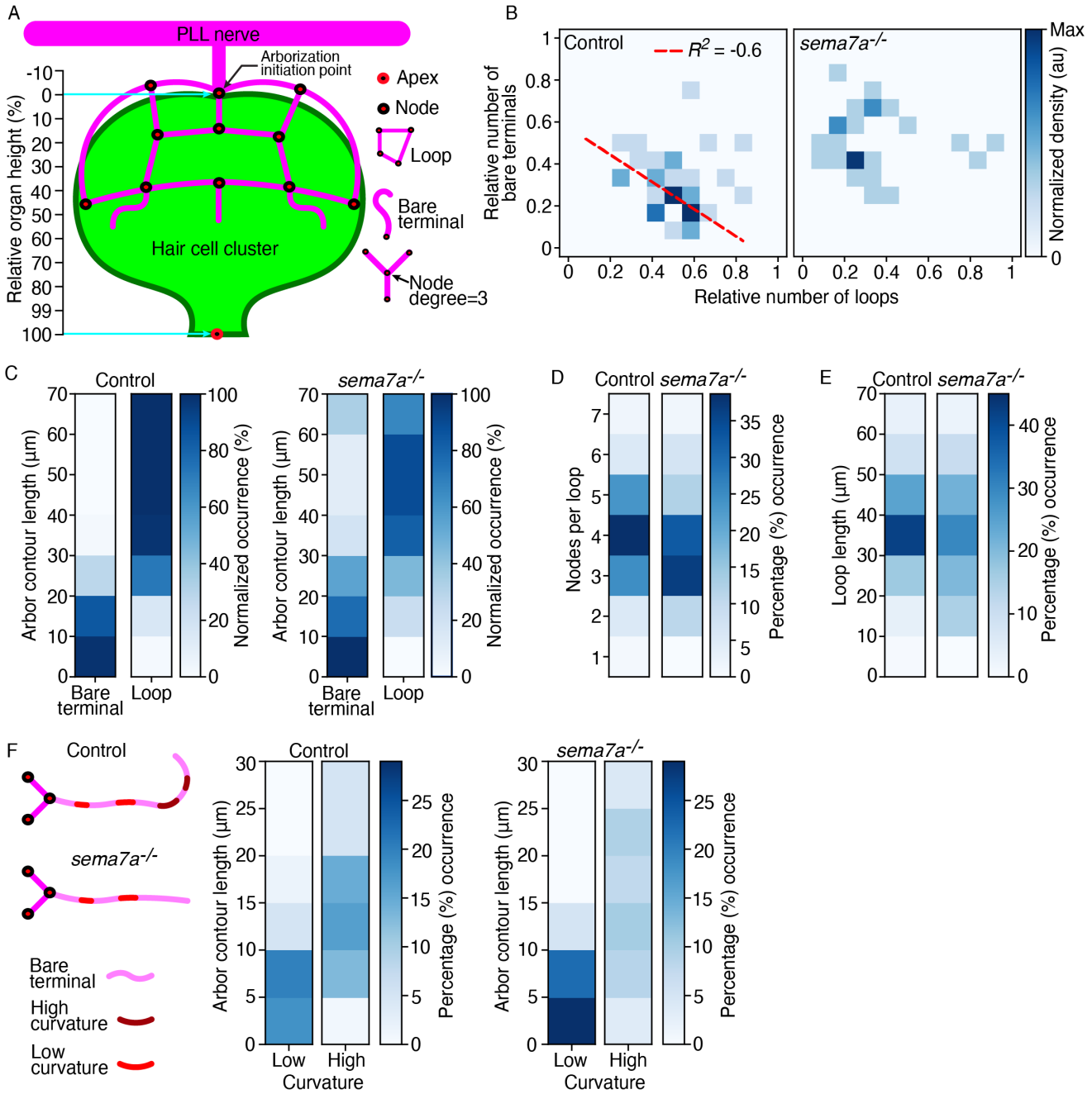

Figure 3. Sema7A patterns the topology of the sensory arbor network. (A) A schematic drawing of the combined hair cell cluster (green) and associated sensory axons (magenta) shows diverse topological features of the arborization network, including nodes, loops, bare terminals, node degree, and bare-terminal curvature. The apex is defined as the center of the hair bundle cluster and the base is denoted by the node from which the arborizations extends. The relative organ height describes the position along the axis formed between the arborization

1030 initiation point and the apex of the hair cell cluster. (B) The correlation between the relative
1031 number of bare terminals and loops from 35 control neuromasts and 27 *sema7a*$^{-/-}$ neuromasts
1032 at 4 dpf shows a negative correlation in the control but a scattered distribution in the mutants.
1033 The same neuromasts were analyzed in the subsequent panels. R^2, correlation coefficient.
1034 Dashed red line depicts the regression slope. (C) The relationship of contour lengths to bare
1035 terminals and loops reveals reduced looping in the mutants. (D) Quantification of the number
1036 of nodes per loop demonstrates a decrease in mutants. (E) Mutants in the same larvae manifest
1037 a broader distribution of loop lengths. (F) A schematic diagram of the extending bare terminals
1038 depicts regions of high and low curvature along the length of the arbor. The distributions of
1039 bare terminals between low- and high-curvature groups show an enrichment of long, highly
1040 curved arbors in the control and short, linear arbors in the mutants. Statistical analyses are
1041 displayed in Table 1.
1042

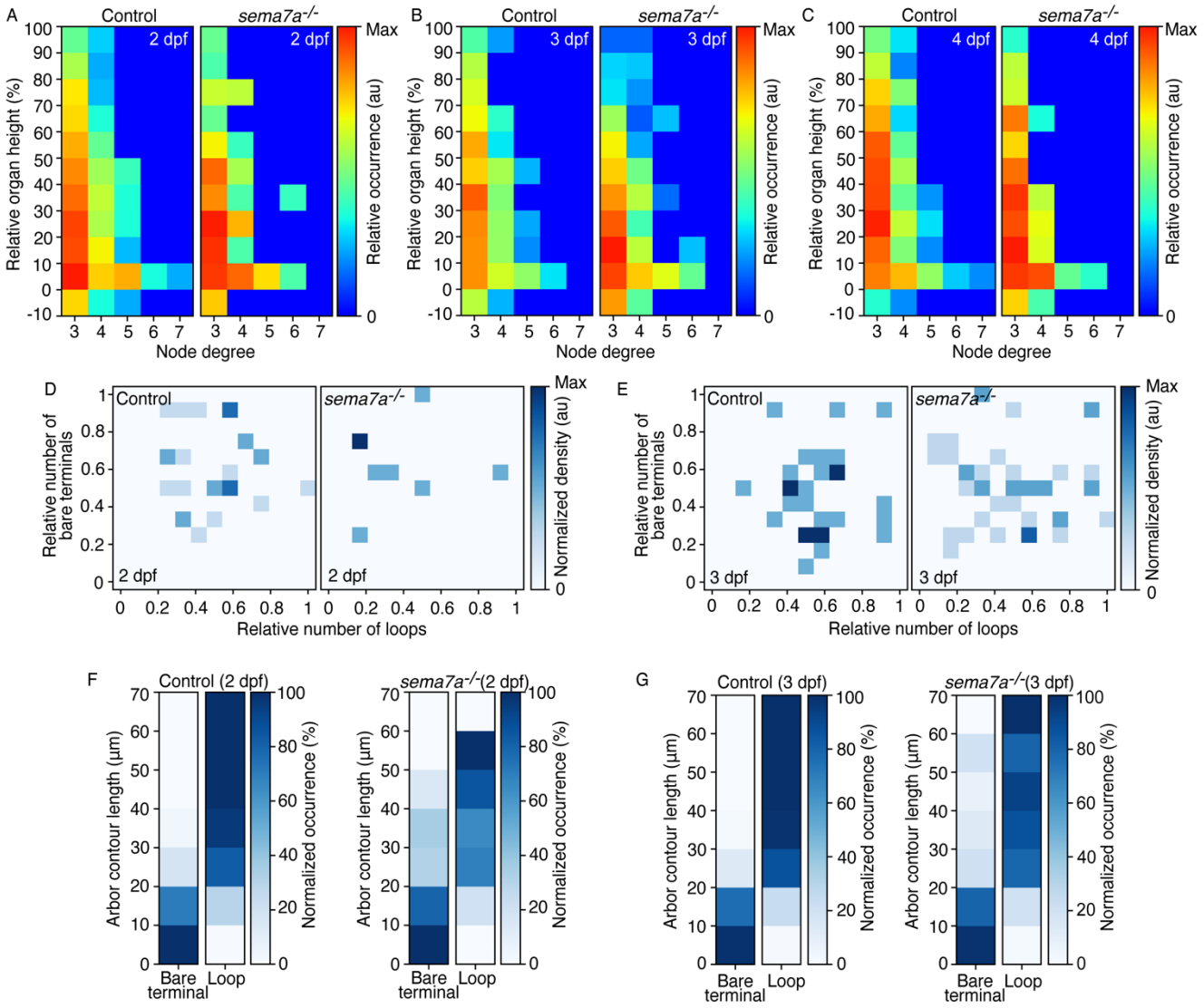

Figure 3—figure supplement 1. Quantification of topological features across developmental stages and genotypes. (A-C) The distribution of node degrees as a function of the height in hair cell clusters shows the difference in the network's hierarchical organization between control and *sema7a*$^{-/-}$ larvae. Nodes of low degree are commonly observed between genotypes across developmental stages (A, B), but their distribution along the cluster height became significantly different at 4 dpf (C), with nodes in control larvae localizing higher along the axis than in the mutants. In this and the following two panels, 33, 29, and 35 neuromasts were analyzed from 2 dpf, 3 dpf, and 4 dpf control larvae, respectively and 17, 53, and 27 neuromasts were analyzed from 2 dpf, 3 dpf, and 4 dpf *sema7a*$^{-/-}$ mutant larvae, respectively (D, E) The correlations between the relative number of bare terminals and loops from control

1053 and *sema7a*$^{-/-}$ neuromasts reveal dispersive distributions at both 2 dpf (D) and 3 dpf (E) stages,
1054 suggesting that the networks are undergoing reorganization and yet to adopt an ordered
1055 topology. (F,G) In the distribution of arbors between bare terminals and loops with respect to
1056 their contour lengths, mutants' arbors display significantly higher propensity to remain as bare
1057 terminals compared to the controls at both 2 dpf (F) and 3 dpf (G). The samples were identical
1058 to those in the previous panel. Statistical analyses are displayed in Table 1.
1059

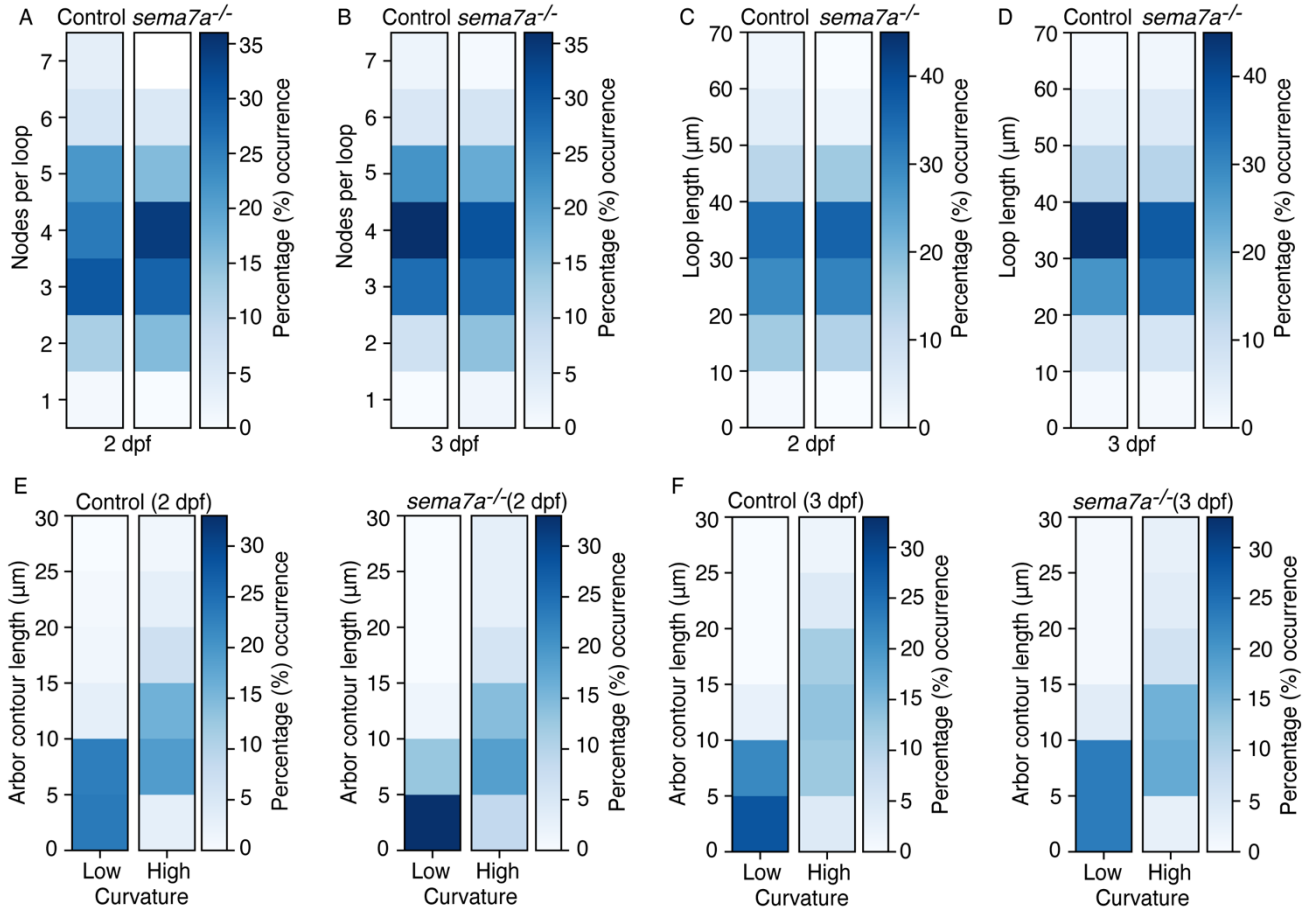

Figure 3—figure supplement 2. Quantification of topological features between control and *sema7a*$^{-/-}$ larvae across developmental stages. (A, B) Quantifications of the number of nodes per loop demonstrate a broader, but not significantly different, distribution in the mutants than the controls at both 2 dpf (A) and 3 dpf (B). In this and the following panels, 33 and 29 neuromasts were analyzed from 2 dpf and 3 dpf control larvae, respectively and 17 and 53 neuromasts were analyzed from 2 dpf and 3 dpf *sema7a*$^{-/-}$ mutant larvae, respectively. (C, D) Quantifications of loop lengths from the same larvae indicate a wider, but not significantly different, distribution in the mutants than the controls at both 2 dpf (C) and 3 dpf (D). (E, F) The distributions of bare terminals between low- and high-curvature groups from the same larvae show higher occurrences of long, curved arbors in the control and short, linear arbors in the mutants at both 2 dpf (E) and 3 dpf (F) stages. Statistical analyses are displayed in Table 1.

Height of node degrees	*p*-values (control vs *sema7a*$^{-/-}$)		
	2 dpf	3 dpf	4 dpf
Degree = 3	3.50E-01	1.05E-08***	1.68E-03**
Degree = 4	3.85E-01	7.11E-02	1.71E-03**
Degree = 5	4.60E-01	5.23E-01	4.40E-01
Bare terminals vs Loop	2 dpf	3 dpf	4 dpf
0 to 10 μm	3.84E-01	7.89E-01	2.11E-01
10 to 20 μm	3.50E-02*	3.92E-01	2.94E-02*
20 to 30 μm	2.28E-04***	2.63E-02*	3.82E-09***
30 to 40 μm	5.04E-59***	3.63E-25***	1.28E-33***
40 to 70 μm	———	———	———
Nodes per loop	5.06E-01	1.96E-01	3.50E-02*
Loop length	5.81E-01	2.71E-01	2.21E-02*
Distribution of bare terminal curvature	2 dpf	3 dpf	4 dpf
	4.23E-01	8.91E-01	1.99E-02*

1072

1073 **Table 1. Statistical comparison between control and *sema7a*$^{-/-}$ larvae for topological**
1074 **features.** One-sided Kolmogorov-Smirnov tests were used to assess the difference in node
1075 degree heights, nodes per loop, and loop lengths for control *versus sema7a*$^{-/-}$ neuromasts at
1076 2 dpf, 3 dpf, and 4 dpf. In each of these cases, the difference in the distributions were not
1077 significantly different (*p*-values in red) between the control and the mutants at 2 dpf and 3 dpf
1078 but became significantly different (*p*-values in green) at 4 dpf. Chi-square tests were used to
1079 assess the difference in occurrences of bare terminals versus loops, as well as the occurrences
1080 of bare terminals with low versus high curvature. The distribution at 4 dpf shows significant
1081 difference between the control and the mutant larvae. The occurrence of significant differences
1082 at 4 dpf for diverse topological features suggest that Sema7A function is required to achieve
1083 an ordered network topology at a mature stage. Thirty-three, 29, and 35 neuromasts were

1084 analyzed from 2 dpf, 3 dpf, and 4 dpf control larvae, respectively, and 17, 53, and 27
1085 neuromasts were analyzed from 2 dpf, 3 dpf, and 4 dpf *sema7a*$^{-/-}$ mutant larvae, respectively.
1086 * Signifies $p < 0.05$, ** signifies $p < 0.01$, and *** signifies $p < 0.001$.
1087

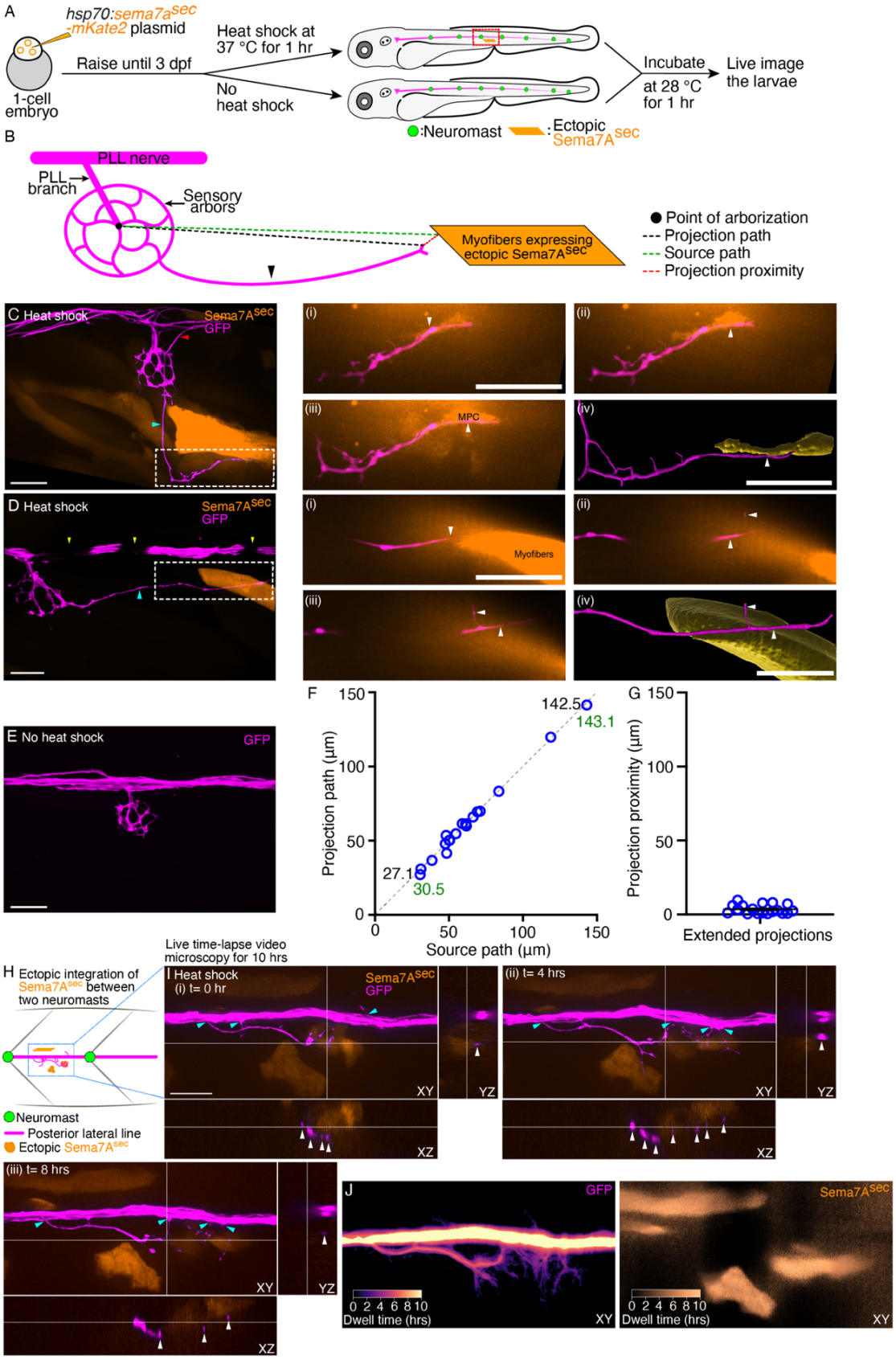

1088 **Figure 4. Ectopic Sema7A^sec diffusive cue provides neural guidance *in vivo*.** (A) A

1089 diagrammatic overview depicts the generation of a transgenic animal that expresses the
1090 Sema7A^{sec} protein ectopically under the control of a thermally inducible promoter. Larvae with
1091 ectopic myotomal-integration near the network of sensory arbors (red rectangle) were imaged
1092 to analyze arbor morphology. (B) A schematic drawing of a sensory arbor from a heat-shocked
1093 larva depicts an extended axonal projection (arrowhead) that reaches toward the myofibers
1094 expressing the ectopic Sema7A^{sec} protein. Parameters that quantitate the accuracy of the
1095 extended axonal projections toward the ectopic Sema7A^{sec} sources are denoted. (C) In a
1096 micrograph of an ectopically expressing Sema7A^{sec} (orange) larva, the sensory arbor
1097 (magenta) extends two aberrant axonal projections. One elongates (cyan arrowhead) along
1098 the somite boundary to reach and contact an ectopically integrated muscle progenitor cell
1099 (white dashed line) and the other (red arrowhead) reenters the posterior lateral-line nerve while
1100 following a second ectopic source. The through-focus scans (i–iii) from the epidermis to the
1101 dermomyotome and the three-dimensional (3D) surface reconstruction (iv) reveal the intimate
1102 contact between the aberrant sensory arbor (arrowheads) and the muscle progenitor cell. (D) In
1103 a micrograph of an ectopically expressing Sema7A^{sec} (orange) larva, the sensory arbor
1104 (magenta) extends a single aberrant axonal process (cyan arrowhead) to reach ectopically
1105 integrated myofibers (white dashed line). The through-focus scans (i–iii) from the epidermis to
1106 the dermomyotome and the 3D surface reconstruction (iv) reveal the proximal association of
1107 the aberrant sensory arbor (arrowheads) to the myofibers. Melanocytes (yellow arrowhead)
1108 along the horizontal myoseptum intermittently block the visibility of the lateral-line nerve. (E) An
1109 injected, but not heat-shocked, control larva does not express ectopic Sema7A^{sec} and does not
1110 show aberrant projection from the sensory arbor. (F) A plot demonstrates the accuracy of 18
1111 extended axonal arbors in finding ectopic Sema7A^{sec} sources. Each circle represents a single
1112 ectopic integration event. The two pairs of numbers represent the minimal and maximal lengths
1113 of the projection path (black) and its corresponding source path (green). (G) A plot quantitates
1114 the distribution of projection-proximity length from 18 ectopic integration events. (H) A
1115 schematic drawing of a section of the lateral-line nerve between two neuromasts from a heat-
1116 shocked larva depicts a few extended neurites (magenta) reaching toward the cells expressing

1117 the ectopic Sema7A^{sec} protein (orange). The Sema7A^{sec} integration site (blue rectangle) with
1118 the sensory axonal projections was imaged for ten hours to visualize axonal dynamics. (I)
1119 Micrographs (i-iii) at three distinct times in the time-lapse video microscopy show directed
1120 branching (cyan arrowheads) of the sensory neurites from the lateral-line nerve toward the
1121 ectopic Sema7A^{sec} sources. Each panel depicts the ectopic integration site and the associated
1122 sensory neurites from three different planes, XY, XZ, and YZ. White arrowheads in XZ and YZ
1123 planes highlight the close association of the sensory axons with the ectopic Sema7A^{sec}
1124 sources. (J) The micrographs depict in pseudocolored trajectories the dwell times of the
1125 sensory neurites (left) at the Sema7A^{sec} sources (right) for ten hours. MPC, muscle progenitor
1126 cell; scale bars, 20 μm; means ± SEMs.
1127

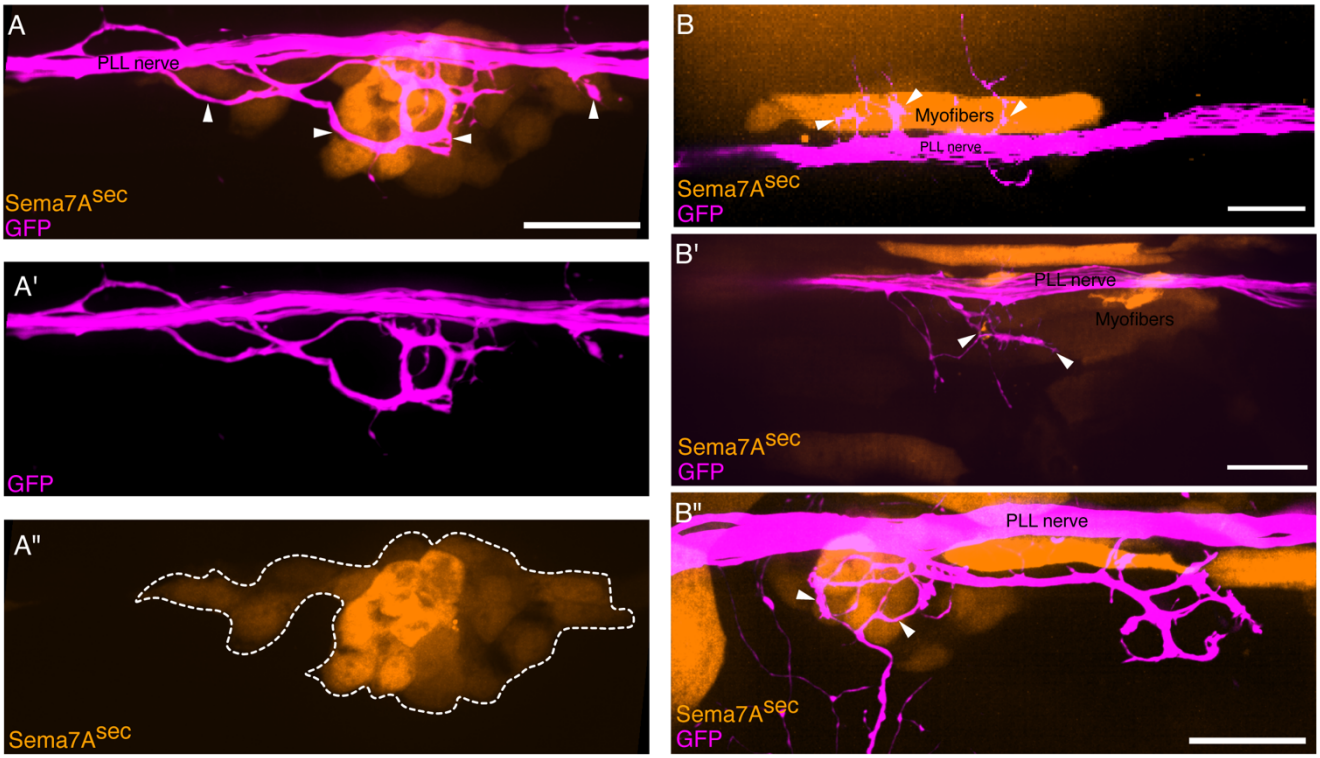

Figure 4—figure supplement 1. Ectopic Sema7A^{sec} diffusive cues induce aberrant sensory neurite extension. (A-A") In a micrograph of an ectopically expressing Sema7A^{sec} (orange) larva, the sensory arbors (magenta) extend multiple axonal projections (arrowheads) that reenter the lateral-line nerve while following an ectopic Sema7A source. Maximal-intensity projections of the sensory arbors and the ectopically expressing Sema7A cells (white dashed line) are shown in A' and A", respectively. (B-B") Micrographs depict three individual incidents of ectopic *sema7a^{sec}* (orange) integrations that occurred distant from neuromasts. In each case, a set of myofibers expresses the ectopic Sema7A^{sec} protein that induces neurite extensions (arrowheads) from the lateral-line nerve (magenta) toward itself. Scale bars, 20 μm.

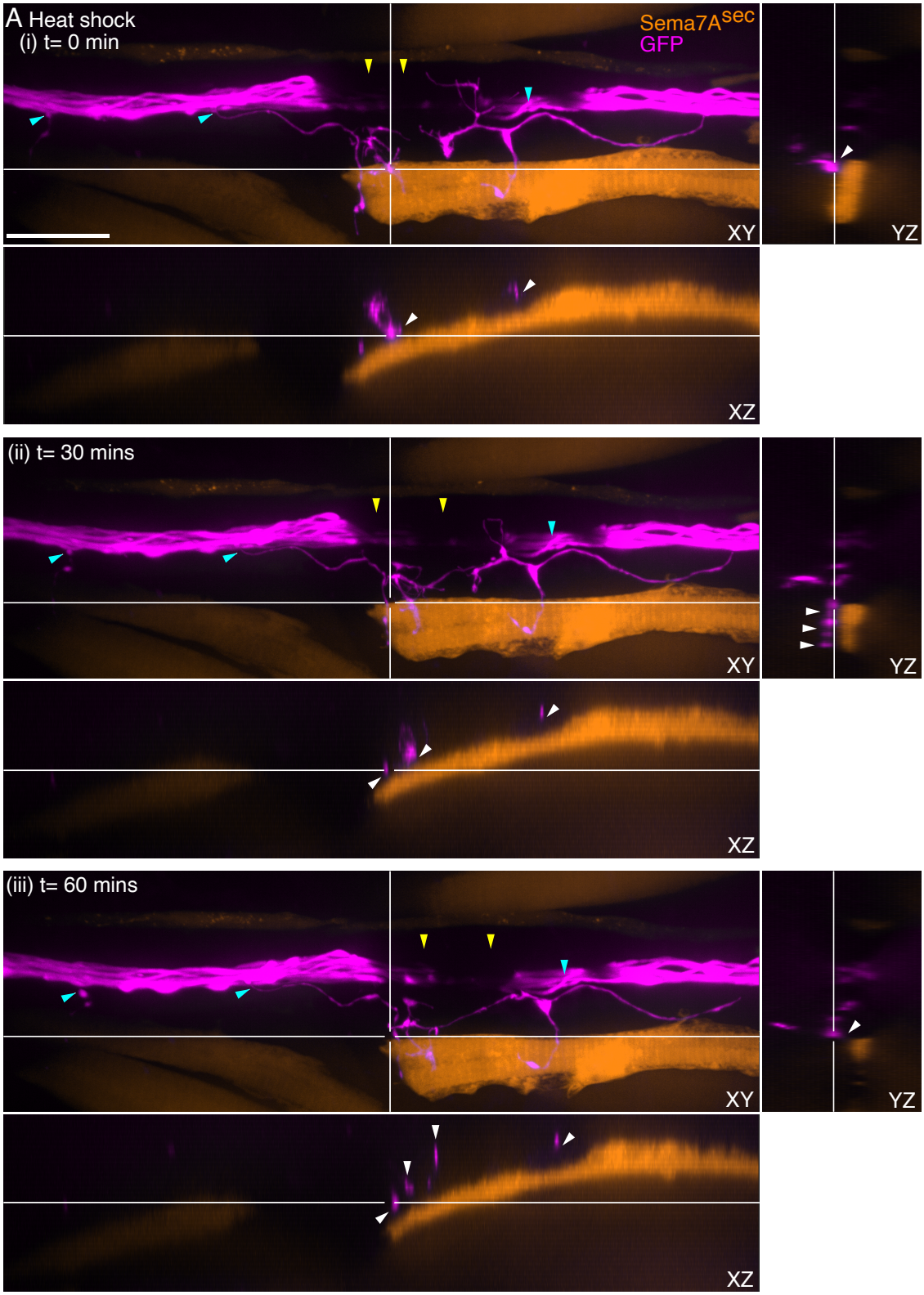

Figure 4—figure supplement 2. Ectopic integration of Sema7A^{sec} distant from the neuromast induces sensory neurite extension. (A) Micrographs of a section of the lateral-line nerve between two neuromasts from a 3-dpf heat-shocked larva depicts a few extended neurites (magenta) reaching toward the cells expressing the ectopic Sema7A^{sec} (orange). The

1143 Sema7A^{sec} integration site with the sensory axonal projections was imaged for one hour to
1144 visualize axonal dynamics. Micrographs (i-iii) at three distinct time-points from the time-lapse
1145 video microscopy show directed branching (cyan arrowheads) of the sensory neurites from the
1146 lateral-line nerve toward the ectopic Sema7A^{sec} sources. Each panel depicts the ectopic
1147 integration site and the associated sensory neurites from three different planes, XY, XZ, and
1148 YZ. White arrowheads in XZ and YZ planes highlight the close association of the sensory axons
1149 with the ectopic Sema7A^{sec} sources. Melanocytes (yellow arrowheads) along the horizontal
1150 myoseptum intermittently block the visibility of the lateral-line nerve. Scale bar, 20 μm.
1151

1152 **Video 5. Sensory axonal projections contact an embryonic muscle progenitor cell**
1153 **expressing Sema7A^{sec}.** A through-focus scan of a 3 dpf larva depicts a muscle progenitor
1154 cell in the dermomyotome that expresses the ectopic Sema7A^{sec} (orange) and the sensory
1155 axonal projection (magenta) that makes intimate contact with it. Scale bar, 20 μm.

1156 **Video 6. Volumetric surface reconstruction of a sensory arbor and an embryonic muscle**
1157 **progenitor expressing Sema7A^{sec}.** Reconstruction of the muscle progenitor cell (orange) at
1158 3 dpf reveals its intimate association with an attracted sensory arbor (magenta).

1159 **Video 7. Volumetric surface reconstruction of a sensory arbor and the mature myofibers**
1160 **expressing Sema7A^{sec}.** Reconstruction of mature myofibers expressing ectopic Sema7A^{sec}
1161 (orange) at 3 dpf shows their close association with the attracted sensory arbors (magenta).

1162 **Video 8. Sensory axonal projections remain in proximity to myofibers expressing**
1163 **Sema7A^{sec}.** A through-focus scan of a 3 dpf larva depicts mature myofibers expressing
1164 exogenous Sema7A^{sec} deep in the myotome (orange) and the sensory axonal projection
1165 (magenta) that remains nearby.

1166 **Video 9. Aberrant axonal projections reenter the lateral-line nerve while following an**
1167 **ectopic Sema7A^{sec} source.** A through-focus scan of a 3 dpf larva depicts cells expressing
1168 exogenous Sema7A^{sec} (orange) that guides the aberrant sensory axonal projection (magenta)
1169 back into the lateral-line nerve. Scale bar, 20 μm.

1170 **Videos 10, 11, and 12. Ectopic Sema7A^{sec} expression induces aberrant neurite**
1171 **projections from the lateral-line nerve.** Through-focus scans of 3 dpf larvae depict three
1172 individual incidents of ectopic *sema7a^{sec}* (orange) integrations that occurred distant from the
1173 neuromasts. In each case, myofibers express ectopic Sema7A^{sec} protein (orange) that attracts
1174 neurite extensions from the lateral-line nerve (magenta). Scale bars, 20 μm.

1175 **Videos 13 and 14. Volumetric reconstructions depict close contacts between the**
1176 **sensory neurites and the ectopic Sema7a^{sec} expressing cells.** Volumetric reconstructions
1177 of 3 dpf larvae depict two individual incidents of ectopic *sema7a^{sec}* (orange) integrations that
1178 occurred distant from the neuromasts. In each case, myofibers or random mosaic of cells in
1179 the dermomyotome express ectopic Sema7A^{sec} protein (orange) that attracts neurite
1180 extensions from the lateral-line nerve (magenta).

1181 **Video 15 and 16. Time-lapse video microscopies depict the dynamics between the**
1182 **sensory neurites and the ectopic Sema7a^{sec} expressing cells.** Time-lapse images of 3 dpf
1183 larvae depict two individual incidents where the ectopic Sema7A^{sec} sources (orange) induce
1184 directed branching of the sensory neurites (magenta) from the lateral-line nerve toward itself.
1185 Within each time-lapse videos, individual panel depicts the ectopic integration site and the
1186 associated sensory neurites from three different planes, XY, XZ, and YZ. Scale bars, 20 μm.
1187

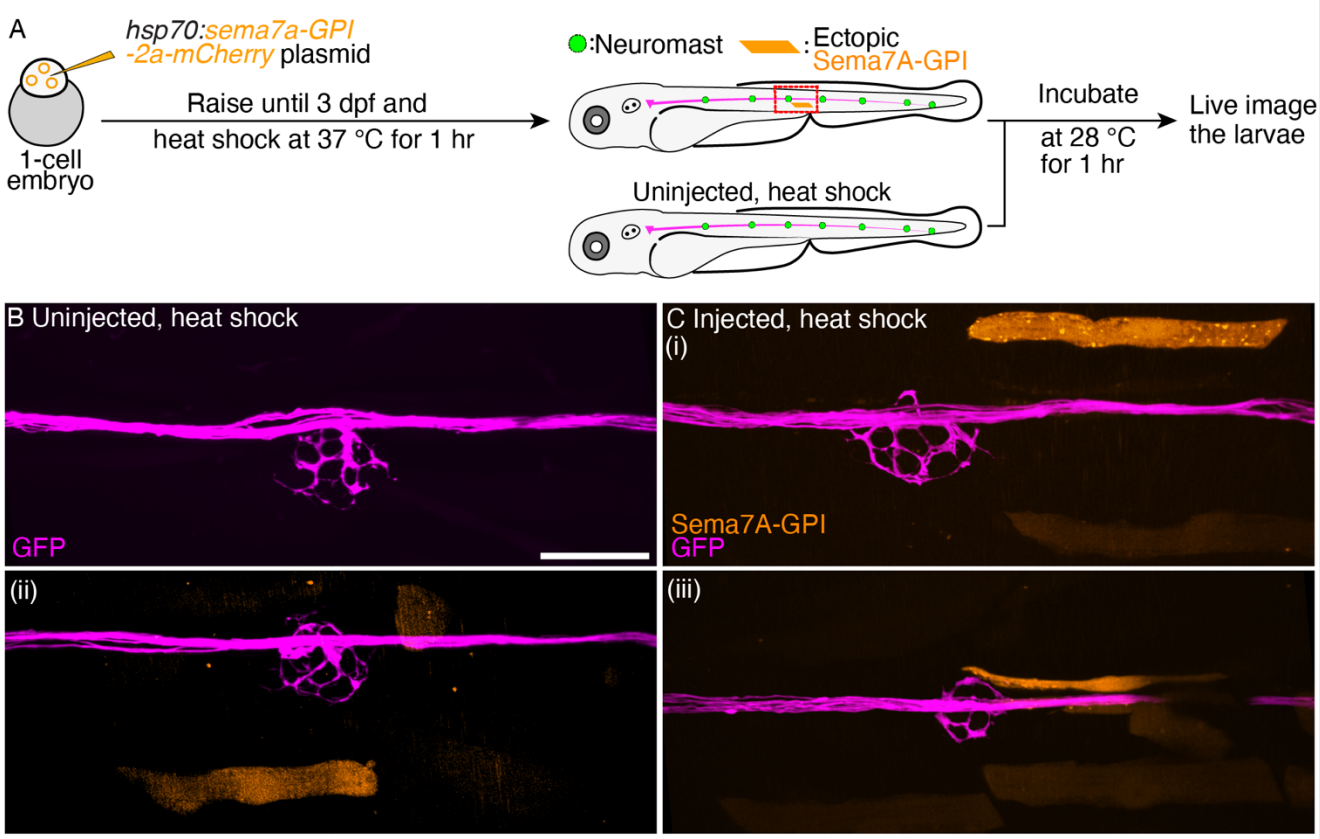

Figure 5. Ectopic Sema7A-GPI fails to guide sensory arbors from a distance. (A) A diagrammatic overview depicts the generation of a transgenic animal that expresses the Sema7A-GPI protein ectopically under the control of a thermally inducible promoter. Larvae with ectopic myotomal-integration near the network of sensory arbors (red rectangle) were imaged to analyze arbor morphology. Uninjected, heat-shocked larvae were used as controls. (B) Uninjected and heat-shocked larva depicts normal arborization pattern of the sensory axons (magenta). (C) Injected and heat-shocked larvae robustly express the Sema7A-GPI in the myofibers (orange). Panels (i-iii) depict the ectopically expressing Sema7A-GPI myofibers that fail to attract sensory arbors toward itself. Scale bar, 20 μm.

1198 **Videos 17, 18, and 19. Sema7A-GPI is incapable to impart sensory axon guidance from**
1199 **a distance.** Through-focus scans of 3 dpf larvae depict three individual incidents of ectopic
1200 *sema7a-GPI* integrations that occurred near the sensory arbor network. In each case,
1201 myofibers robustly express ectopic Sema7A-GPI protein (orange) but the sensory arborization
1202 pattern (magenta) remain unperturbed. Scale bars, 20 μm.
1203

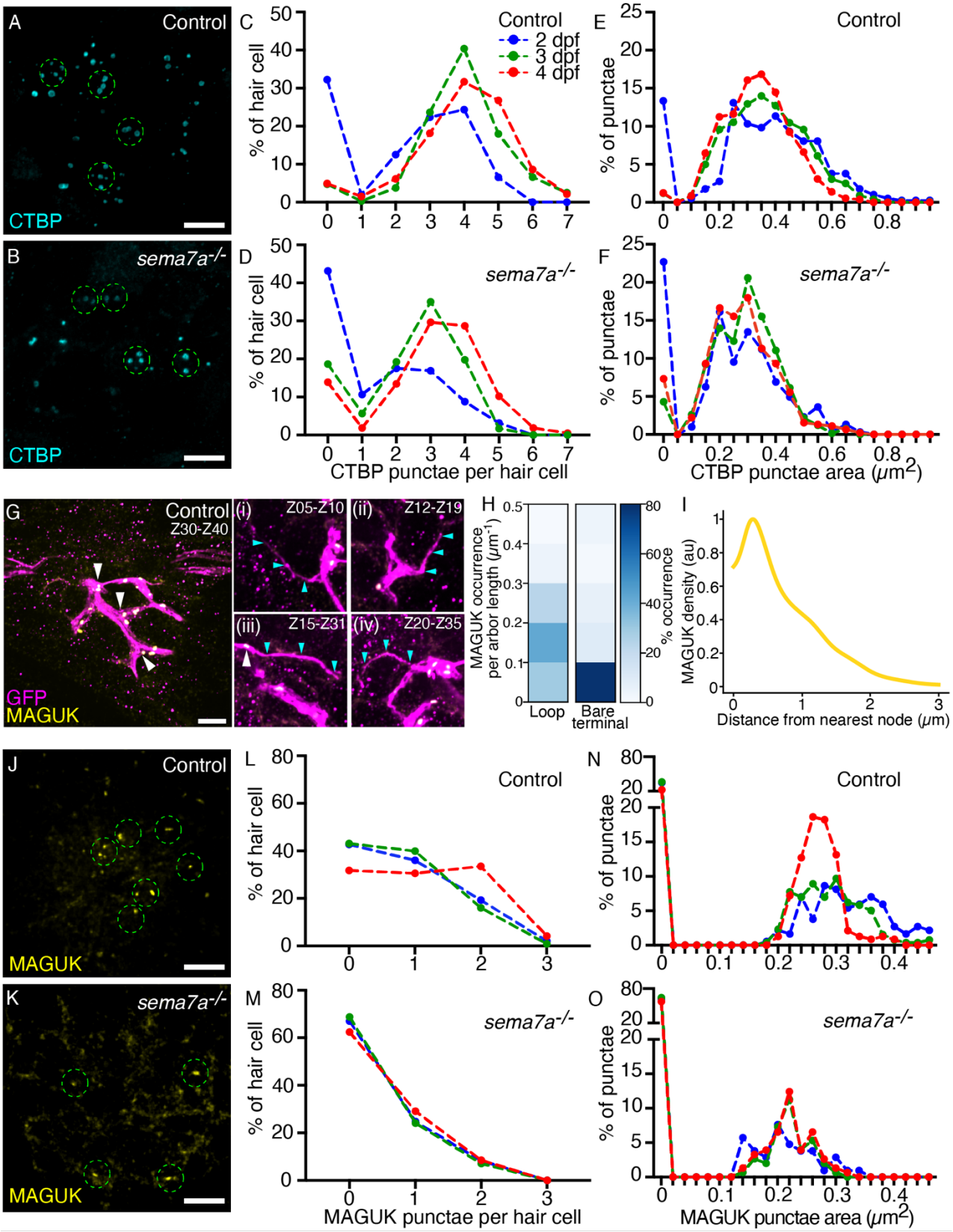

1204 **Figure 6. Sema7A deficiency impairs synaptic assembly.** (A,B) Maximal-intensity

1205 projections of micrographs from a control and a *sema7a*$^{-/-}$ neuromast depict the presynaptic
1206 aggregates marked by CTBP (cyan). The approximate hair cell basal region is outlined by
1207 dashed green circles. (C-F) Plots quantitate the numbers of presynaptic aggregates (C,D) and
1208 their areas (E,F), in each hair cell across developmental stages. One hundred and fifty-two,
1209 317, and 325 hair cells were analyzed from 2 dpf, 3 dpf, and 4 dpf control larvae, respectively.
1210 One hundred and sixty, 216, and 177 hair cells were analyzed from 2 dpf, 3 dpf, and 4 dpf
1211 *sema7a*$^{-/-}$ mutant larvae, respectively. (G) A micrograph generated from maximal-intensity
1212 projection of ten consecutive through-focus scans across Z-planes of a control 4 dpf neuromast
1213 depict the sensory arbors (magenta) and the postsynaptic aggregates marked by MAGUK
1214 (yellow, white arrowheads). The MAGUK punctae primarily occur on the loop and aggregate
1215 near the nodes. Panels (i-iv) depict maximal-intensity projection of consecutive through-focus
1216 scans of distinct Z-planes to show bare terminals. In each panel, the bare terminal (magenta,
1217 cyan arrowheads) rarely harbors postsynaptic aggregates (yellow, white arrowhead). (H)
1218 Quantification of the distribution of the MAGUK-punctae between the two topological features
1219 of the network depicts enrichment of postsynaptic densities on the loops over the bare
1220 terminals. (I) A histogram shows the distribution of MAGUK-punctae density against the
1221 distance from the node. The histogram is represented as a density trace graph (yellow). For
1222 both H and I, five hundred and sixty-seven MAGUK punctae were analyzed from 16
1223 neuromasts of 4 dpf larvae. (J,K) Maximal-intensity projections from micrographs of a control
1224 and a *sema7a*$^{-/-}$ neuromast depict the postsynaptic aggregates marked by MAGUK (yellow).
1225 The approximate hair cell basal region is outlined by dashed green circles. (L-O) Plots
1226 quantitate the numbers of postsynaptic aggregates (L,M) and their areas (N,O), in each hair
1227 cell across developmental stages. One hundred and fifty, 218, and 167 hair cells were analyzed
1228 from 2 dpf, 3 dpf, and 4 dpf control larvae, respectively. Ninety-seven, 141, and 141 hair cells
1229 were analyzed from 2 dpf, 3 dpf, and 4 dpf *sema7a*$^{-/-}$ mutant larvae, respectively. Scale bars,
1230 5 μm.
1231

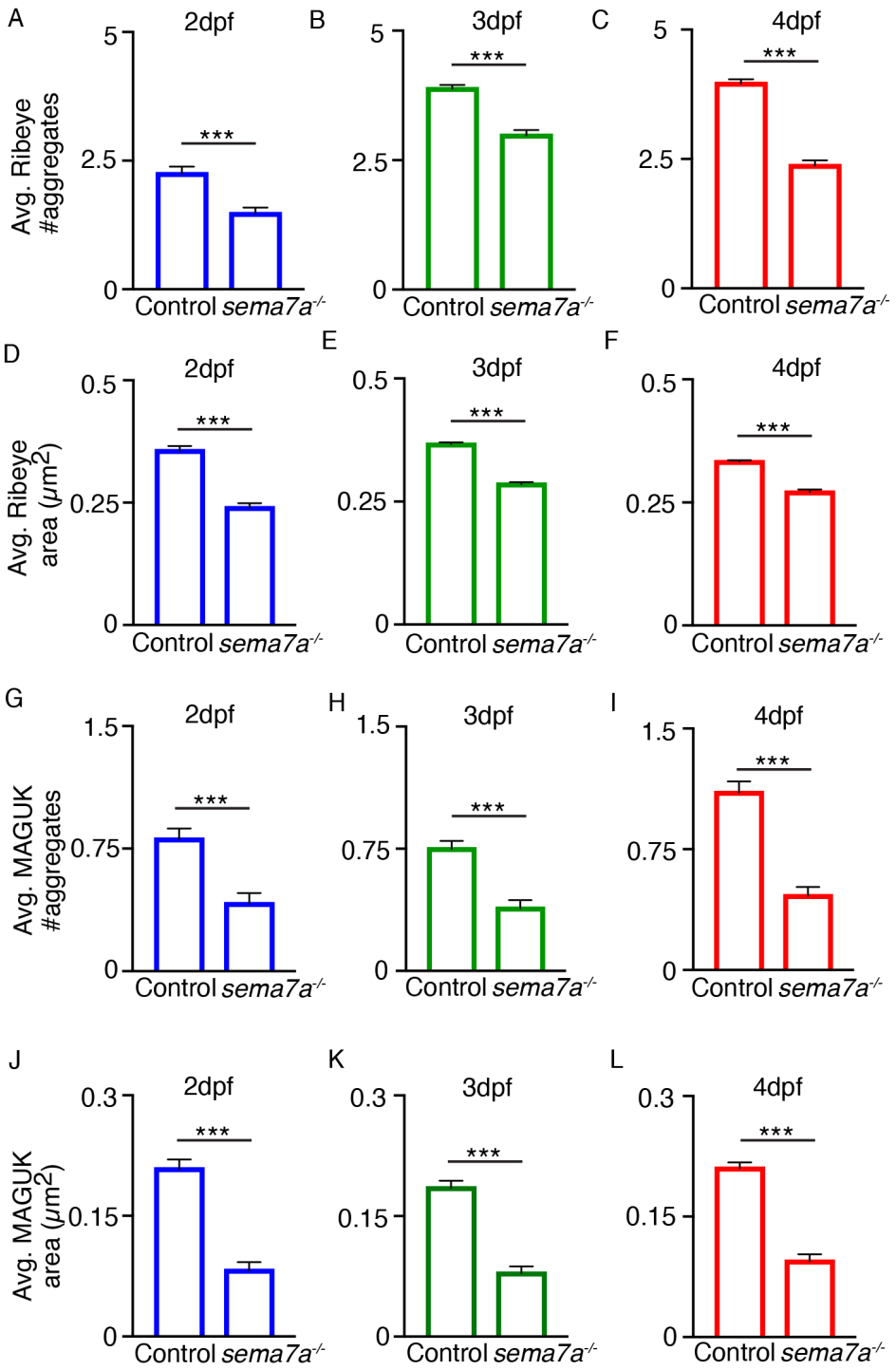

Figure 6—figure supplement 1. *sema7a*$^{-/-}$ mutants display impaired synaptic assembly. (A-F) The plots quantitate the average numbers and areas of presynaptic aggregates from control and *sema7a*$^{-/-}$ neuromasts. Significant decreases in the numbers and areas of presynaptic aggregates are observed across development. Three hundred and forty-one, 1229,

1237 and 1286 presynaptic aggregates were analyzed from 2 dpf, 3 dpf, and 4 dpf control larvae,
1238 respectively. Two hundred and thirty-five, 643, and 419 presynaptic aggregates were analyzed
1239 from 2 dpf, 3 dpf, and 4 dpf *sema7a*$^{-/-}$ mutant larvae, respectively. (G-L) The plots quantitate
1240 the average numbers and areas of postsynaptic aggregates from control and *sema7a*$^{-/-}$
1241 neuromasts. Significant decreases in the numbers and areas of postsynaptic aggregates
1242 occurred during development. Three hundred and ninety-seven, 1243, and 1300 postsynaptic
1243 aggregates were analyzed from 2 dpf, 3 dpf, and 4 dpf control larvae, respectively. Three
1244 hundred and four, 651, and 451 postsynaptic aggregates were analyzed from 2 dpf, 3 dpf, and
1245 4 dpf *sema7a*$^{-/-}$ mutant larvae, respectively. Means ± SEMs; *** implies $p < 0.001$.
1246

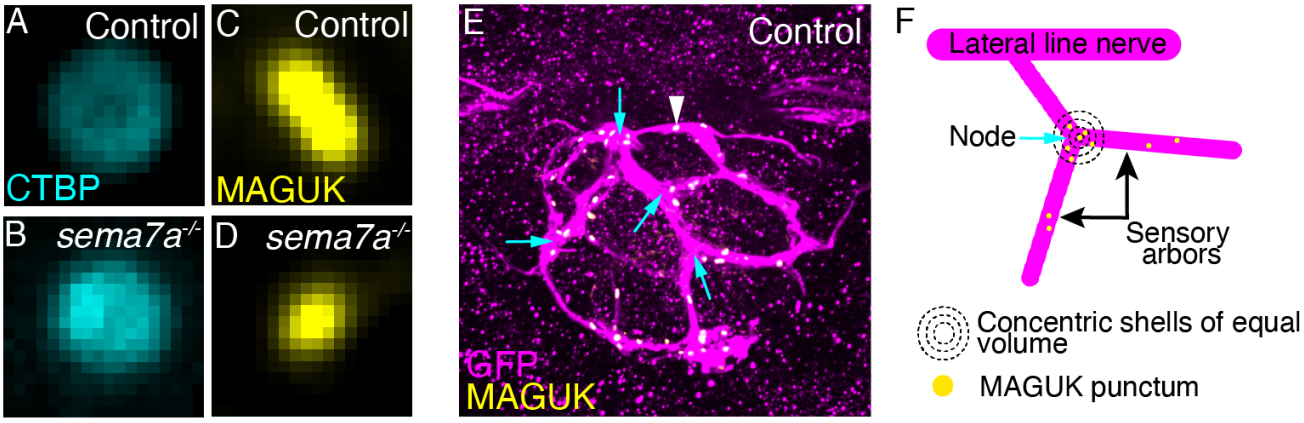

Figure 6—figure supplement 2. Morphologies of presynaptic and postsynaptic assemblies and the distribution of postsynaptic aggregates across the sensory arbor network. (A,B) The micrographs depict single presynaptic aggregate marked by CTBP in control (A) and in sema7a-/- mutant (B) larvae at 4 dpf. (C,D) The micrographs depict single postsynaptic aggregate marked by MAGUK in control (C) and in sema7a-/- mutant (D) larvae at 4 dpf. (E) A maximal-intensity projection micrograph depicts the sensory arbor network (magenta) and the enrichment of the postsynaptic assemblies (yellow, white arrowhead) near the nodes (cyan arrows). (F) A schematic diagram of the sensory arbor network depicts the enrichment of the MAGUK punctae near the node (cyan arrow). The three-dimensional space surrounding each node was divided into concentric shells of equal volume to measure the distribution of MAGUK-punctae density across the network.

1259 **Video 20. Postsynaptic assemblies are enriched in the loops and near the nodes of a**
1260 **sensory arbor network.** Through-focus scans of a 4 dpf neuromast depict the sensory arbor
1261 network (magenta) where the postsynaptic assemblies (yellow) are primarily located in the
1262 loops of the arbor network and are enriched near the nodes.
1263

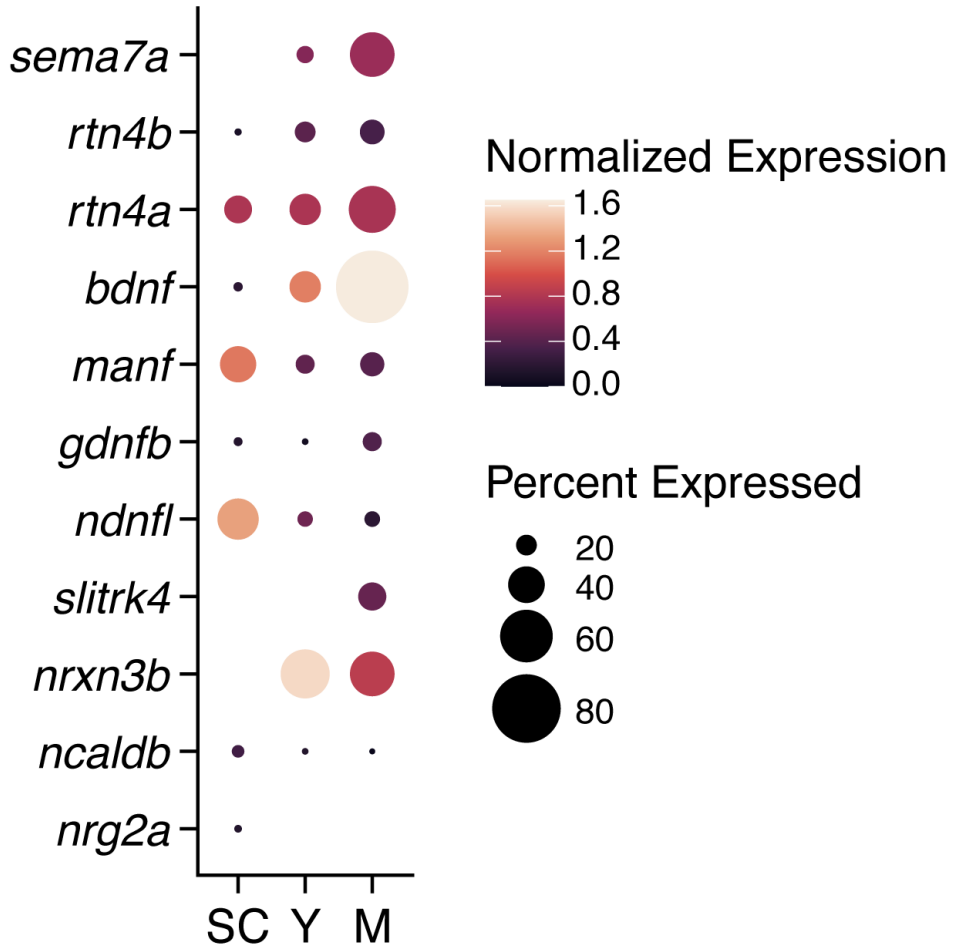

Figure 7. Expression of diverse neural guidance cues in developing neuromasts. Analysis of single cell RNA-sequencing data (9) shows the expression of multiple neural guidance genes that are expressed across young hair cells (Y), mature hair cells (M), and support cells (SC). Dot sizes and colors signify the proportion of cells in each cluster that express a gene and the average strength of expression (log[(counts/10,000) +1]), respectively.